A REAL-TIME DIGITAL HOLOGRAPHIC MICROSCOPE WITH AN OPTICAL TWEEZER

by

Mert Doğar

Submitted to the Graduate School of Engineering and Natural Sciences
in partial fulfillment of
the requirements for the degree of
Master of Science

Sabancı University

August 2014

A REAL-TIME DIGITAL HOLOGRAPHIC MICROSCOPE WITH AN OPTICAL TWEEZER

APPROVED BY:

Assoc. Prof. Dr. Meriç Özcan, (Dissertation Supervisor)

.....

Assoc. Prof. Dr. Ayhan Bozkurt

.....

Assoc. Prof. Dr. Erkay Savaş

.....

DATE OF APPROVAL: ...03.09.2014

Abstract

The most significant advantage of the holographic microscopy is being able to image transparent objects such as biological cells without staining. Therefore, the cell image can be captured while it is alive. Moreover, Manipulating a living cell without destructing it's structure can be achieved by the use of an optical tweezer which apply a pulling force around a tightly focused laser beam without a physical contact. Therefore, an instrument that combines the holographic microscope and the optical tweezer is quite useful for biological studies.

Another advantage of holographic imaging is that, one does not need to do mechanical focusing for the scene when recording the hologram. Focusing is achieved by reconstructing the hologram at a certain depth. If the object's optical depth from the recording plane is not known a priori, auto-focusing algorithms must be used to estimate this distance. However, auto-focusing and reconstruction can be quite time consuming as the hologram sizes increase and the microscope can not operate in real-time with high resolution holograms using traditional central processing units (CPUs). Therefore, for real-time operation, additional hardware accelerators are required for reconstructing high resolution holograms. A holograms can be reconstructed tens of times faster with a graphics processing unit than with the state-of-the-art main CPUs.

In this thesis, an auto-focusing megapixel-resolution digital holographic microscope (DHM) that uses a commodity graphics card as the calculation engine is presented. The computational power of the GPU allows the DHM to work in real-time such that the reconstruction distance is estimated unsupervised, and the post-processing of the hologram is transparent to the user. Performances of the DHM under GPU and CPU settings are presented and a maximum of 70 focused reconstructions per second (frps) are achieved with 1024×1024 pixels holograms. Moreover, a

setup for incorporating an optical tweezer to the holographic microscope is provided. With this setup, it is possible to trap small particles while performing holographic imaging.

Abstract (Türkçe Özet)

Holografik mikroskopların en önemli özelliği, biyolojik hücreler gibi şeffaf nesnelerin resimlerinin, nesneleri boyamaya gerek olmaksızın kaydedilebilmesidir. Bu sayede, hücreler canlıyken incelenebilmektedir. Bunun yanında, canlı hücreleri taşımak yada hapsetmek için odaklanmış lazer ışını ile çalışan bir optik cımbız kullanilabilir. Dolayısıyla, optik cımbız ve holografik mikroskobu bir araya getiren bir araç biyoloji çalışmalarında oldukça yararlı olacaktır.

Holografikde, kayıt esnasında mekanik odaklama yapılmasına gerek yoktur. Kaydedilen hologramın içindeki belirli parçacıklara odaklamak için doğru uzaklıkta yeniden yapılandırma yapmak gerekir. Yeniden yapılandırma, hologram yuzeyindeki dalga dağılımını sayısal olarak yayarak elde edilir. Eğer parçacığın kayıt yüzeyine olan optik uzaklığı bilinmiyorsa, bu uzaklığı tahmin etmek için otomatik odaklama yöntemleri kullanılmalıdır. Ancak, hologramın boyutu büyük olduğunda otomatik odaklama ve yeniden yapılandırma işleri uzun zaman almaktadır. Dolayısıyla, yalnızca bilgisayar işlemcileri kullanarak yüksek çözünürlüklü sayısal holografik mikroskobu gerçek zamanlı çalıştırmak olanaksızdır. Mikroskopu gerçek zamanlı çalıştırmak için donanımsal hızlandırıcılara ihtiyac duyulmaktadır. Günümüz tüketici grafik kartları genel amaçlı hızlandırılmış işlem yapmaya çok müsaittirler. Bu kartlar kullanıldığında, hologramlar en gelişkin işlemcilere nazaran onlarca kat daha hızlı bir şekilde yeniden yapılandırılabilirler.

Bu tezde; otomatik odaklama yapabilen yüksek çözünürlüklü bir sayısak holografik mikroskop (DHM) tanıtılmaktadır. Grafik kartının getirdigi işlem gücü ile mikroskop, gerçek zamanlı otomatik odaklama ve hologram işleme yeteneğine sahip olmustur. GPU kullanıldıgında saniyede 70 tane 1024×1024 boyutunda hologramın otomatik odaklama ile yeniden yapılandırılabildiği gösterilmiştir. Ayrica, optik cımbız ile sayısal holografik mikroskobu birleştiren bir düzenek önerilmektedir. Bu düzenek ile bir yandan örneğin 3 boyutlu görüntüsü kaydedilirken diğer yandan optik cımbız ile hapsedilmesi ve taşınması gösterilmiştir.

Acknowledgements

I would like to express my gratitude to my supervisor Assoc. Prof. Dr. Meriç Özcan for the useful comments, remarks and engagement through the learning process of this master thesis. His world view always inspired me. I would like to thank to my thesis defense committee members Assoc. Prof. Dr. Ayhan Bozkurt and Assoc. Prof. Dr. Erkay Savaş for their interest and constructive criticisms.

Furthermore, I would like to thank to my colleague A. Hazar İlhan. This thesis would not be written without his contribution. Together, we overcome several difficulties.

I appreciate the support of The Scientific and Technological Research Council of Turkey (TÜBİTAK) for this project under the research fund No:110T613.

Finally, I would like to thank my family, who have supported me throughout entire process, both by keeping me harmonious and helping me putting pieces together. I will be grateful forever for your love.

TABLE OF CONTENTS

List of Tables

List of Figures

1 INTRODUCTION

Holography is a technique for obtaining the complex wave-field of an electromagnetic wave. The technique was invented by a Hungarian electrical engineer Gabor [1] in 1948 while he was working on improving the resolution of the electron microscopy. In his original manuscripts, the technique was named as wavefront-reconstruction, but afterwards it is called holography. The word holography comes from two Greek words 'holos' and 'graphen' which mean 'whole' and 'to write' respectively. Holography requires coherent light source, since the technique uses an interferometer where the amplitude and the phase properties of a wave-field are transformed into a non-complex image. Gabor realized that by using a coherent light source and with a proper recording setup, the phase and amplitude of the original object wave can be reconstructed later. He conducted experiments with visible light of a filtered mercury arc. However, the coherence of such a source, his holograms were restricted to transparencies little larger then a pinhead. The lack of a well coherent source restricted the progress of holography at early stages until the invention of lasers.

In 1959, Gould published an article that describes an open resonator to achieve highly coherent source. His notes include several possible application of a coherent source such as spectroscopy, interferometry and radar [2]. The appearance of laser and increase in the coherence length of sources gave holography the impetus it needs. Around 1962, the first commercial helium-neon lasers became available, and Leith and Upatnieks started recording more assertive holograms. They divided the laser light to illuminate the object and to use as reference, and they experimented with off-axis holograms where the angle between the object beam and the reference beam

is slightly greater than zero [3].

The same year, Denisyuk introduced thick holograms which can be reconstructed using white light [4]. Within a few years, holography started to be used in many real world applications such as vibration analysis, surface coating analysis and deflection measurements [5, 6, 7].

In 1969, Brown and Lohman synthesized digital holograms on computers which became a game changing approach for the holography [8]. Later in 1970s, as computers started to improve rapidly, not only the hologram synthesis but also the hologram reconstruction was started to be performed on computers [9, 10]. This eliminated the necessity of using a physical reference light in reconstructions and established a new perspective which later led to the idea of digital holography. In 1994, Schnars and Jüptner showed that the charge-coupled devices (CCD) can be used for recording digital holograms [11]. However, the real-time processing is not possible when the size of the holograms increase to several mega-pixels range, because hologram processing complexity is proportional to the resolution of the hologram. In 2004, Lenart presented an accelerated data-path and a processing unit which utilizes a field programmable gate array (FPGA) to reduce the reconstruction time [12, 13]. In same year, Shimobaba et al. introduced a parallelized high-performance computing board for computer-generated hologram, named HORN-5. HORN-5 was equipped with four large-scale FPGAs and it was 360 times faster then a Pentium 4 CPU [14]. Although FPGA based methods seem quite beneficial for processing large holograms, those methods have high engineering and equipment costs when compared to graphics cards. Today, commodity graphics cards can provide the required computational power for doing the reconstruction [15, 16] and auto-focusing in real-time [17].

In addition, holography is used for many other applications such as 3D imaging [18, 19], refractive index measurements [20], imaging through turbid [21, 22, 23],

holographic data storage [24, 25] and holographic display research [26]. Those topics are not directly related to this thesis and they are not covered.

Microscopy is one of the most important applications of the digital holographic microscopy [27, 28, 29, 30, 17]. As opposed to conventional imaging techniques, using a single hologram, holography provides focused images of particles that are located at different depths inside the microscope slide. Moreover, even though the particles are transparent, their 3D information is obtained numerically.

Besides, an optical tweezer can be incorporated in the digital holographic microscope in order to trap and manipulate the particles while imaging them in 3D. The optical tweezers were first introduced by Ashkin in 1970, where a focused laser beam was used for trapping [31] small particles. Since, the particles are manipulated remotely without having a physical contact; the optical tweezers are convenient instruments for bio-science experiments.

In this thesis, the concept of the auto-focusing megapixel-resolution digital holographic microscope (DHMs) is presented. Two digital holographic microscopes have been constructed where commodity graphics card are utilized for accelerating the hologram processing. In addition, the second microscope includes an optical tweezer that enables particle trapping and holographic imaging simultaneously. The rest of the thesis is organized as follows:

In the second chapter, the principles of holography is explained. Moreover, the hologram recording, filtering, reconstruction and auto-focusing methods are covered. In the third chapter, hologram reconstruction and auto-focusing with commodity graphics cards are explained. Then, the speed-up achieved by using a graphics card as opposed to a traditional processor is discussed. In the fourth chapter, the notion of a real-time auto-focusing digital holographic microscope is introduced and the working principles of such a microscope is presented. In the fifth chapter, our approach for

incorporating an optical tweezer in the the digital holographic microscope is explained and the experimental results are provided. Finally, the conclusion and the future directions provided by this thesis are summed up in the chapter six.

2 HOLOGRAPHY

A hologram is the interference pattern of a reference wave and an object wave. In order to obtain 3D information of the object, the hologram must be filtered and reconstructed with a proper reference wave. In this chapter; hologram recording, filtering, reconstruction and auto-focusing are covered.

2.1 Hologram Recording

Current recording devices are not able to record the complex properties of the light wave. They respond to the intensity variations of the wavefront. Therefore, the phase information somehow must be converted into intensity variation over the recording media. This is done via an interferometer.

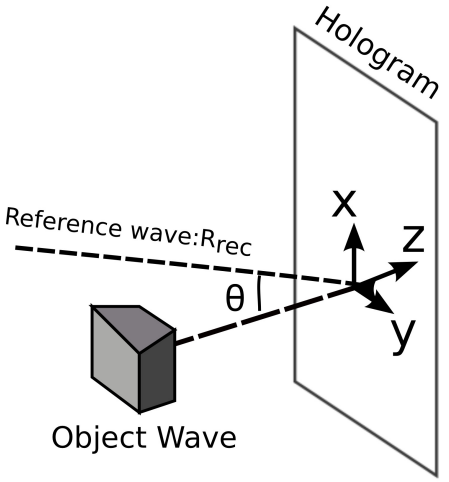

Figure 2.1: Hologram recording setup

In an interferometer, a coherent light source (laser) is split into two beams, then those two beams are used for object illumination and reference wave as in figure 2.1.

There are two types of hologram recording techniques: transmission mode and reflection mode. In transmission mode, the object beam passes through the specimen and later it interferes with the reference beam on the recording plane. Similarly, in the reflection mode, the object is illuminated with the object beam, and the scattered wave interferes with the reference beam on the recording plane in order to form the hologram. The interference pattern which appears over the recording medium is mathematically expressed as:

$$I = O + R, \tag{2.1}$$

where O is the object wave and R is the reference wave. The most important concern regarding the quality of the interference is the contrast of the pattern. To achieve a maximum interference, the difference of distance traveled by two branches of the recording setup must be smaller than the coherence length of the light source (laser). In addition, polarization quality of the laser and mechanical stability of the recording device are critical for better holograms.

In recording stage, the intensity of the interference pattern is recorded on a 2 dimensional medium:

$$H = |I|^2 = |O + R|^2, \tag{2.2}$$

where H is the hologram image. Assuming the light source is coherent, the equation 2.2 can be expressed as:

$$H = (O + R) \cdot (O + R)^* = |O|^2 + |R|^2 + OR^* + O^*R, \tag{2.3}$$

where * is the complex conjugate operator. Although the phase of the interference pattern is lost in the recording stage, the equation contains the complex object wave O.

The equation 2.3 is interpreted as sum of three terms such as zero order image, object image and conjugate image. Zero order image is the non-complex part of the

equation ($|O|^2 + |R|^2$). On the other hand, the object and the conjugate images are complex terms and they carry the object's 3 dimensional information somehow multiplied by some spatially invariant reference signal. It is better to choose a plane reference wave R to ease up the reconstruction:

$$R = R_0 \cdot e^{-jk \cdot r}, \tag{2.4}$$

where k is the wave-number vector and r is the position vector describing the observation point in space. As a result, the multiplications with the reference wave are simplified to a multiplication with a constant term.

2.2 Hologram Filtering

In order obtain the complex object wave, the zero order image and the conjugate image must be filtered. There are several techniques for filtering these extraneous terms such as the spatial filtering and the phase shifting methods.

2.2.1 Spatial Filtering

The simplest way for hologram filtering is the spatial filtering method. Figure 2.2 shows an off-axis hologram (a) and 2D Fourier transform of the hologram (b) of a man image. When no spatial filtering is applied (Fig. 2.2-c), the zero-order image distorts the object image.

In off-axis configuration, the angle between the reference wave and the object wave is slightly greater than zero. The there dots on figure 2.2-b correspond to the zero order image, conjugate image and the object image. The zero-order image is at the center, and the position of the object and the conjugate images shift proportional to the recording angle θ. Thus with off-axis holograms, it is relatively easy to isolate object image O with a simple spatial filtering in the Fourier domain [32]. However, as

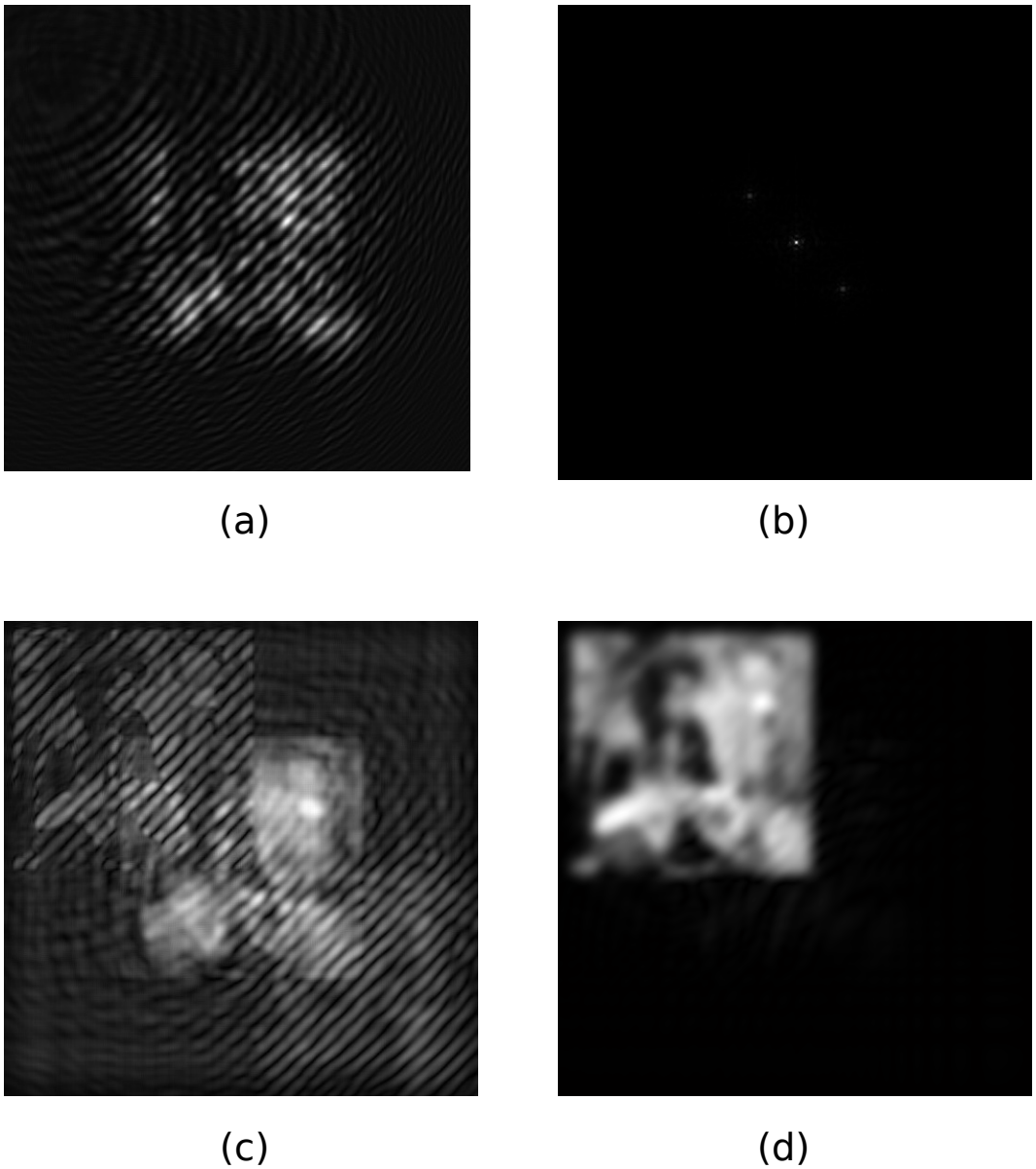

Figure 2.2: Figure shows an off-axis hologram of a man figure (a) and 2D Fourier transform of the hologram (b). The image (c) is the reconstruction without the spatial filtering. After the spatial filter is applied, the reconstruction (d) is obtained.

shown in figure 2.2-d, the resolution of the reconstruction reduces, and it is not desirable for most application. On the other hand in on-axis holograms, the resolution of the reconstruction is maximum. However, all three terms ($OR^*, O^*R, |O|^2+|R|^2$) are super-imposed onto each other spatially. As illustrated in figure 2.3-b, the zero order image occludes the other images. Moreover, all image components are superimposed on the Fourier domain and they cannot be separated with spatial filtering.

2.2.2 Phase Shifting Holography

In order to filter the extraneous images in on-axis holography, one has to resort a more sophisticated filtering method such as phase shifting holography [27, 33] which requires three separate holograms with discrete phase-shift on the reference beam.

In phase shifting holography, pure object wave O can be numerically derived by combining multiple holograms recorded with specific phase shifts on the reference wave. In the simplest case, three holograms are captured with reference waves with 0, $\frac{\pi}{2}$ and π phase shifts and the following equations are obtained:

$$H_0 = |O+R|^2 = |O|^2 + |R|^2 + OR^* + O^*R, \tag{2.5}$$

$$H_{\frac{\pi}{2}} = |O + Re^{j\frac{\pi}{2}}|^2 = |O|^2 + |R|^2 - jOR^* + jO^*R,$$

$$H_\pi = |O + Re^{j\pi}|^2 = |O|^2 + |R|^2 - OR^* - O^*R.$$

Solving the above equations for the object wave O yields the following equation:

$$O = [\frac{1}{4}(H_0 - H_{\pi/2}) + j\frac{1}{4}(H_{\pi/2} - H_0 - H_\pi)] \cdot R, \tag{2.6}$$

where O is the far field of the object wave, and it needs to be propagated for a focused image of the object.

Figure 2.3-a shows an on-axis hologram of a man figure. Before applying phase-shifting holography technique, the reconstruction is distorted (Fig. 2.3-b) due to

super-position of zero-order image, object image and conjugate image. After applying phase-shifting holography technique for filtering the extraneous components, the image (c) is obtained. When we compare the resolutions of figure 2.2-d and figure 2.3-c, we see that on-axis holograms yield better resolution reconstructions.

There are also different phase-shifting approaches. For instance, parallel phase-shifting methods offered in [34, 35, 36] do not require multiple hologram captures. Therefore, in theory it is easier to implement a real-time system using a phase-shifting array. However, the usage of the phase shifting array introduces aberrations. Although some experimental results are presented in the papers, strict requirement of alignment makes the method impractical.

2.3 Reconstruction of Digital Holograms

At first, holograms were being recorded on photographic plates or films. The recording process took very long time to develop a single hologram. A major break-through was happened after the explosion of electronic devices such as computers and digital cameras. In 1994, Schnars and Jüptner showed that charge-coupled devices (CCDs) can be used for recording digital holograms [11]. The interference pattern is digitally recorded via a CCD or CMOS sensor and the hologram is stored as a 2D image on a computer. Now, a hologram can be digitally recorded with a camera and reconstructed on a computer even without using a laser in reconstruction. If the properties of the reference wave is well known, the complex wave properties on the object plane can be calculated by propagating the wave-field on the sensor plane through the object plane. Electromagnetic wave diffraction is numerically expressed with the famous Rayleigh-Sommerfeld diffraction integral [33]:

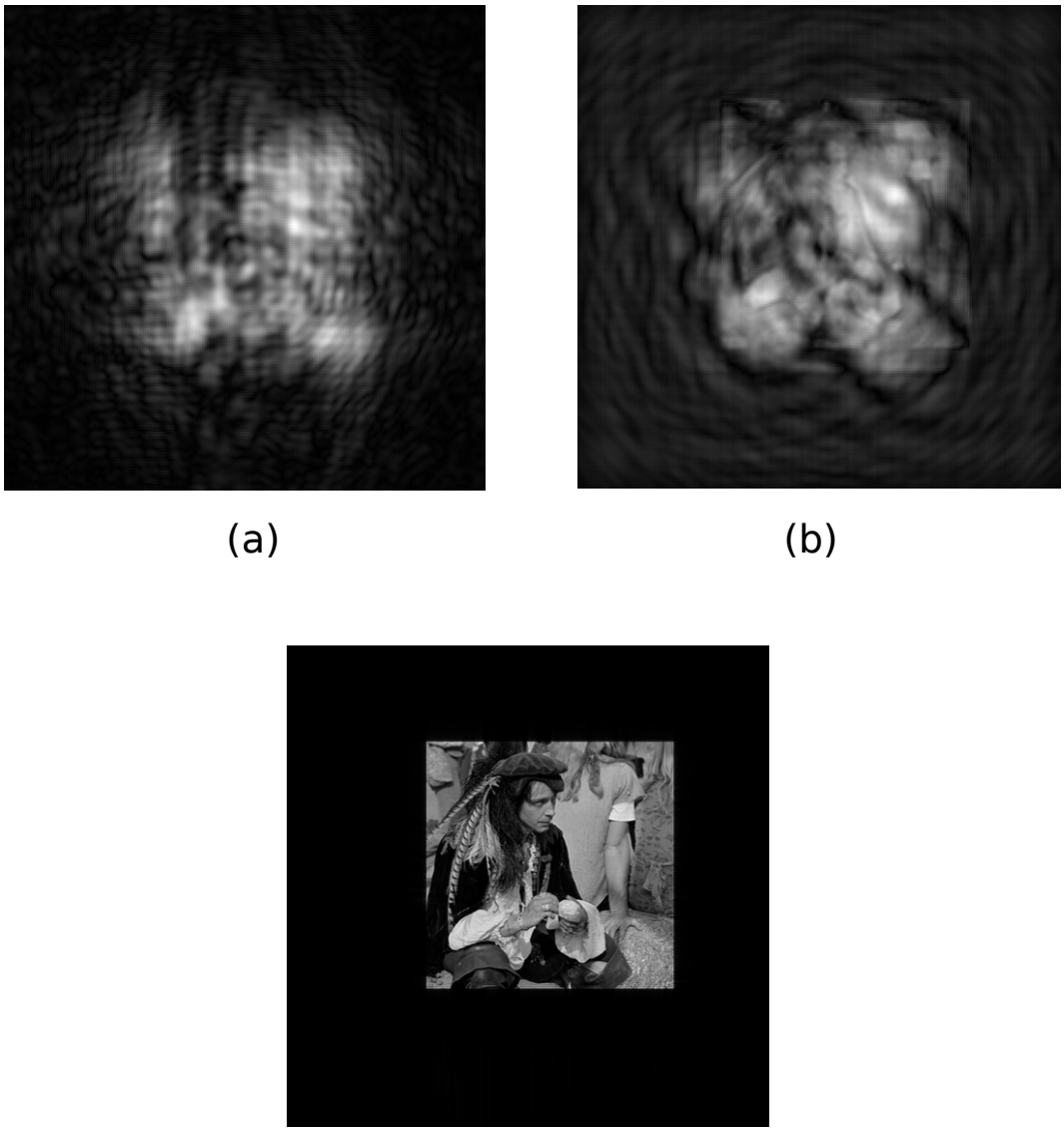

Figure 2.3: Figure shows an on-axis hologram of a man figure (a). (b) is the reconstruction of the hologram at the true focus distance. However, the man image is distorted due to super-position of zero-order image, object image and conjugate image. After applying phase-shifting holography technique for filtering the extraneous components, the image (c) is obtained. As can be seen, the resolution of the reconstruction is much higher than the reconstruction obtained in off-axis configuration.

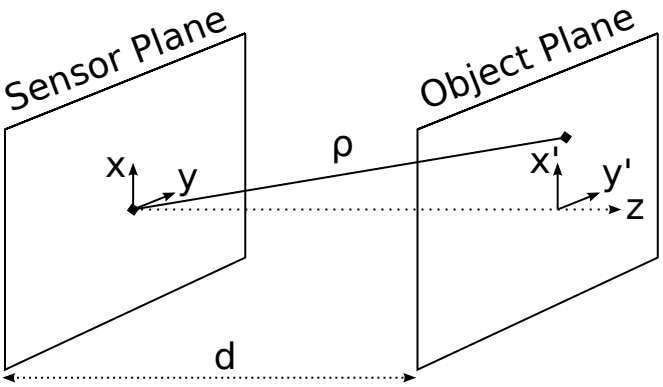

Figure 2.4: The figure shows the coordinate system used in our mathematical calculations where d is the distance of propagation, (x, y, x', y') are the coordinate system parameters and ρ is the distance between the points in sensor plane and object plane. In our case, the field distribution over the sensor plane is recorded as a hologram and propagation is performed on the z-axis.

$$U_d(u,v) = \frac{1}{i\lambda} \int\int U_0(x,y)\, \frac{exp(-i2\pi\rho/\lambda)}{\rho}\, cos\theta\, dx\, dy\,, \tag{2.7}$$

where U_0 is the wave distribution on the sensor plane, $\rho = \sqrt{d^2 + (x-x')^2 + (y-y')^2}$ is the distance between the points on the sensor plane and object plane, λ is the wavelength of the electromagnetic wave and $\cos\theta$ is the obliquity factor [19].

Using this formulation, wave pattern at any plane parallel to the hologram's aperture can be numerically obtained by simply evaluating the Rayleigh-Sommerfeld diffraction integral. However, the complexity of evaluating the Rayleigh-Sommerfeld integral over a big sized hologram is tremendous so that it becomes impractical to use Rayleigh-Sommerfeld's equation in real life applications. For this reason, approximate versions of the Rayleigh-Sommerfeld are used in order to reduce the computational power required for a single hologram reconstruction. These approximations have certain limitations and constraints. In following sections, three most common hologram reconstruction methods will be explained.

2.3.1 Fresnel approximation

The most common way of doing a reconstruction is the Fresnel method. When the propagation distance is big enough compared to the object dimensions, the distance term ρ in the denominator of the Rayleigh-Sommerfeld integral can be substituted by d, the distance for propagation. However, basic replacement of ρ in the numerator can cause big errors since it is in a phase term. Therefore, ρ in the numerator is subsituted by it's second order binomial expansion [Eq. 2.8].

$$\rho = d + \frac{((x-x')^2}{2d} + \frac{(y-y')^2}{2d}. \tag{2.8}$$

Under Fresnel approximation, the obliquity factor, $\cos\theta$ converges to 1 and the Rayleigh-Sommerfeld integral turns to [19, 11, 33]:

$$\begin{aligned} U_d(x',y') =& \frac{1}{i\lambda d}\ exp(\frac{-i2\pi d}{\lambda})\ exp(\frac{-i\pi}{\lambda d}(x'^2+y'^2)) \\ & \int\int U_0(x,y)\ exp(\frac{-i\pi}{\lambda d}(x^2+y^2))\ exp(\frac{i2\pi}{\lambda d}(xx'+yy'))\ dx\,dy. \end{aligned} \tag{2.9}$$

A simplified interpretation of (2.9) can be written as [37, 11]:

$$U_d(x',y') = Q_i(x',y')\ \int\int U_0(x,y)\ Q_O(x,y)\ exp(\frac{i2\pi}{\lambda d}(xx'+yy'))\ dx\,dy \tag{2.10}$$

where $Q_i(x',y')$ and $Q_O(x,y)$ are called as quadrature terms. This equation can be treated as a 2D inverse Fourier transformation when d goes to infinity and that verifies the Fraunhofer region properties [33]. Therefore the field distribution over the object plane is obtained using a 2D inverse Fourier transformation and point-wise multiplication with the quadrature terms.

In discrete domain, the Fresnel's method is expressed as:

$$U(m,n) = Q_i(m,n) \sum_{k=-N_x/2}^{N_x/2-1} \sum_{l=-N_y/2}^{N_y/2-1} U_o(k,l)\, Q_O(k,l)\, exp(i2\pi(\frac{km}{N_x} + \frac{ln}{N_y})), \tag{2.11}$$

where Q_i and Q_o are the discrete quadrature terms as shown respectively:

$$Q_i(m,n) = exp[-\pi\lambda d(\frac{m^2}{N_x^2\Delta x^2} + \frac{n^2}{N_y^2\Delta y^2})], \tag{2.12}$$

$$Q_o(m,n) = exp[-i\frac{\pi}{\lambda d}(k^2\Delta x^2 + l^2\Delta y^2)]. \tag{2.13}$$

The use of Fresnel's method changes the axial properties of the image. This can be a significant disadvantage for applications that analyze a particle in multiple depths. Each reconstruction will have different magnification level; therefore a correction procedure must be applied for matching dimensions at each reconstruction. That brings an extra work which will be a major disadvantage in the real-time systems since the correction should be performed many times in a second.

2.3.2 Convolution method with free-space propagation

There is another formulation for electromagnetic wave propagation that uses convolution theorem for calculating the object wave. If we model the propagation of light in free space as a linear system, the diffraction integral can be expressed as a convolution integral:

$$U_d(x',y') = \int\int U_0(x,y)\ g(x,y,x',y')\ dx\,dy, \tag{2.14}$$

where $g(x,y,x',y')$ is the impulse response of the free-space [37, 38]:

$$g(x,y,x',y') = \frac{i\ exp(\frac{-i2\pi}{\lambda}\sqrt{d^2+(x-x')^2+(y-y')^2})}{\lambda\ \sqrt{d^2+(x-x')^2+(y-y')^2}}. \tag{2.15}$$

The impulse response in equation (2.16) is space-invariant and thus the equation (2.14) turn into a convolution formulation [11]. In discrete domain the impulse response

$g(x, y, x', y')$ is expressed as:

$$h(k,l) = \frac{i}{\lambda} \frac{exp(-i\frac{2\pi}{\lambda}\sqrt{d^2 + (k - N_x/2)^2\Delta x^2 + (l - N_y/2)^2\Delta y^2}}{\sqrt{d^2 + (k - N_x/2)^2\Delta x^2 + (l - N_y/2)^2\Delta y^2}}. \tag{2.16}$$

Convolution approach can be carried out with double sum however the complexity of the system becomes $O(N^4)$. On the other hand, according to the convolution theorem, convolution of two signals can be obtained using the Fourier transform:

$$U_d(x', y') = FT^{-1}(FT(\, U_0(x, y)\,) \times FT(\, g(x, y, x', y')\,)). \tag{2.17}$$

Doing the calculation with Fourier transforms significantly reduces the complexity down to $O(N^2 log(N))$. However, there is a difference between linear convolution and Fourier based convolution. The size of diffraction pattern calculated by linear convolution is $(2N-1) \times (2N-1)$ pixels for a $N \times N$ pixels hologram and the central $N \times N$ pixels of the reconstructed image is the actual result. However in FFT based convolution approach, unless there is nothing done prior to the FFT, the convolution operation with FFT will produce images with $N \times N$ pixels. This is because the FFT operation is cyclic and the result will be the circular convolution. To properly carry out the linear convolution operation, input image has to be padded with zeros to bring the input image size to $(2N-1) \times (2N-1)$ pixels (similarly the size of $h(k, l)$ has to be padded with zeros to bring the size of $h(k, l)$ to $(2N - 1) \times (2N - 1)$ pixels). Then the calculation with FFT method will produce again $(2N - 1) \times (2N - 1)$ pixel image result and again the central $N \times N$ portion of the image is the actual result. Then computational complexity of the convolution method with FFT is $O[(2N - 1)^2\ log_2(2N - 1)]$.

As opposed to the Fresnel method, axial dimensions are not changed with convolution method. Therefore, dimensions of objects stay unchanged at each reconstruction.

This is an advantage for systems that make several reconstructions in different depth and try to identify or locate a particle inside.

Unfortunately, convolution method in discrete domain brings some limitations on propagation distance because of the discrete Fourier transformations involved. In discrete domain, the propagation distance d is constrained with a lower-bound of $d_{min} = N_x \Delta m^2/\lambda$, where Δm is the pixel width and N_x is the pixel count in an axis.

2.3.3 Angular Spectrum

A third method for reconstructing holograms is the angular spectrum method. Angular spectrum of a complex wave on a plane is defined as the Fourier transform of the wave itself with direction cosines of the wave vector being the transform variables:

$$A(u, v; 0) = \iint_{-\infty}^{\infty} O(x, y; 0) e^{-j2\pi(ux+vy)} dx\, dy. \tag{2.18}$$

Here we assume the wave is propagating in the z direction, $O(x, y; 0)$ is the wave at $z = 0$ location, and $u = \alpha/\lambda$ and $v = \beta/\lambda$ are the transform variables in terms of the wavelength λ, and the direction cosines α and β of the wave vector with respect to x and y axes. Propagation along the z-axis is achieved by shifting the phases of all the plane waves of the angular spectrum $A(x, y; 0)$,

$$A(u, v; z) = A(u, v; 0)\, e^{j\frac{2\pi z}{\lambda}\sqrt{1-(\lambda u)^2-(\lambda v)^2}}, \tag{2.19}$$

and back transforming to the spatial domain with inverse Fourier transform [19, 17]:

$$O(x, y; z) = \iint_{-\infty}^{\infty} A(u, v; z)\, e^{j2\pi(ux+vy)} du\, dv. \tag{2.20}$$

The overall procedure is summarized as:

$$T(u, v) = \begin{cases} e^{j\frac{2\pi z}{\lambda}\sqrt{1-(\lambda u)^2-(\lambda v)^2}}, & \sqrt{u^2+v^2} < \frac{1}{\lambda} \\ 0, & otherwise \end{cases} \tag{2.21}$$

$$O(x, y, z) = F^{-1}[F(O(x, y, 0))T(u, v)], \tag{2.22}$$

where F denotes Fourier transform and $T(u, v)$ denotes the transfer function which modulates the angular spectrum of $O(x, y, 0)$.

Discrete implementation of the equation (2.22) consists of two DFTs and a point-wise multiplication with a transfer function $T(u, v)$ [39]. The method has an overall complexity of $\mathcal{O}(N^2 logN)$ for an image with $N \times N$ pixels wide, and as N increases, the computational cost of the angular spectrum method becomes significant.

2.3.4 Comparison of Reconstruction Methods

Previously, three different hologram reconstruction methods are covered. Each of them has constraints and can be preferable under certain conditions. For example, if the reconstruction distance is greater than the object dimensions, Fresnel method gives accurate results and consumes shorter time with respect to others. In discrete domain, Fresnel method consists of only one inverse Fourier transform and two point-wise matrix multiplication. However, in microscopy, the propagation distances are small for relatively small structures, and the Fresnel approximation fails. Luckily, angular spectrum method does not enforce any limitations onto the reconstruction distance; hence a reconstruction is possible even in the micrometer range. The implementation of angular spectrum method consists of one discrete Fourier transform, one discrete inverse Fourier transform and one point-wise matrix multiplication. Similarly, convolution method is also realized using two discrete Fourier transforms and a point-wise matrix multiplication. Fast Fourier transform (FFT) is a computational method for calculation discrete Fourier transform on computers and a 2D FFT operation has a complexity of $O(N^2 \log N)$ where N is the pixel count in one axis.

2.3.5 Auto-focusing

In order obtain a focused image of the specimen, the optical distance of the specimen to the camera plane must be known a priori to the reconstruction. If this distance is not correct even on the order of sub-millimeters, the reconstruction will appear out of focus. There are several focus distance estimation techniques for conventional images and some of those techniques are applicable to the digital holograms. The focus quality of a reconstruction can be evaluated by a sharpness estimation function which produces extreme values as the reconstruction distance approaches to the actual focus distance [28, 40, 41]. To pick the actual focus distance of the reconstruction without a prior knowledge, the hologram must be reconstructed at several distances over an interval and the image with the highest quality must be chosen. There are several focus metrics in image processing literature [42, 29, 43, 28, 41, 44] which are used in holography. Therefore, sharpness estimation functions can be used to compare the quality of reconstructions of a hologram at arbitrary distances. The most common sharpness metric used in holography is the normalized-variance sharpness measure. This method relies on the fact that the magnitude images of the focused reconstructions will yield higher contrast than out-of-focus reconstructions. The normalized-variance measure is expressed as [42, 28]:

$$M_{var} = \frac{1}{\mu} \sum \sum [|O(x,y)| - \mu]^2, \tag{2.23}$$

where μ is the mean of the magnitude of object image. The sharpness curve is formed by plotting image quality measures against the reconstruction distances. An exemplary sharpness curve obtained from a hologram of 1951 USAF resolution chart is shown in figure 2.5.

The sharpness estimation process described above has complexity of $\mathcal{O}(MN^2 logN)$

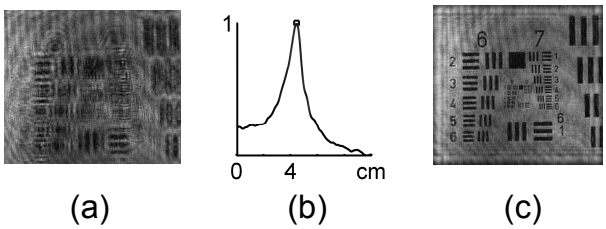

Figure 2.5: Auto-focusing steps are shown on a hologram of USAF resolution chart. The hologram is scaled four times to 128×128 pixels and the new hologram (a) with pixel dimensions $30\mu m \times 30\mu m$ is obtained. Then, the sharpness curve in the middle (b) is calculated by using normalized-variance as the quality metric. Finally, the original hologram is reconstructed at the distance corresponding to the peak of the curve and the object image (c) is obtained.

for an image with $N \times N$ pixels where M is the number of discrete steps on the interval. It is clear that a reduction in the hologram size would significantly increase the performance of the focus distance search. The scaling of holograms with ratio k is defined as dividing the hologram into $k \times k$ squares, and using the average of each square as the pixels of the new scaled hologram. As a result of this operation, pixel dimensions of the this new hologram is also k times larger. In total, the reconstruction of the new hologram will be approximately $k^2 log\, k$ times faster compared to the original [40]. Although the computational cost is reduced significantly as the k increases, the maximum amount of scaling that can be applied without diverging from the true focus distance is limited by the initial size and frequency content of the recorded hologram. The amount of scaling that is applied before the auto-focusing algorithm highly affects the accuracy of sharpness functions as well as the speed of the overall system. In a real-time working set-up, the scaling ratio k should be chosen as large as possible. In our experiments, we find that eight times scaling on mega-pixel size holograms provides sufficient speed-up for real-time operation and it is also robust for continuous unsupervised estimation of the focus distance.

3 GRAPHICS PROCESSORS

In a conventional processor, the real-time reconstruction is not possible when the size of the holograms increase to several mega-pixels range. There are several attempts to improve the reconstruction performance in literature. Lenart (2004) presented a accelerated data-path and a processing unit which utilizes a field programmable gate array (FPGA) to reduce the reconstruction time [12, 13]. In same year, Shimobaba et al. introduced HORN-5 which was a parallelized high-performance computing board for computer-generated hologram. HORN-5 was equipped with four large-scale FPGAs and it was 360 times faster then a Pentium 4 CPU [14]. However, FPGA based methods have high engineering and equipment costs when compared to graphics cards.

Today, graphics cards can provide the required computational power for doing the hologram reconstruction and auto-focusing in real-time. The rapid developments in commodity graphics card technology provide an opportunity to process large blocks of data in a very short amount of time which reduces the hologram processing time significantly. Shimobaba et al. was the first who used graphics card for computing Fresnel's method [15]. Later, Ahrenberg extended their research by including the convolution method and they compared the convolution method with the Frenel's method [16]. Moreover in an earlier work ours, we implemented the angular spectrum method on GPUs and provided the comparison of the three methods [39].

In this chapter, hologram reconstruction and auto-focusing with commercial graphics cards are covered. Then, the speed-up achieved by using a graphics card as opposed to a traditional processor is discussed.

3.1 GPU for General Purpose Computing

A graphics processing unit (GPU) is an electronic equipment inside a graphics cards and they are designed for processing massive chunks of data in parallel. GPUs are composed of hundreds of physical processors and a high bandwidth memory. Although state-of-the-art CPUs perform up to a hundred billion floating point operations per second (GFLOPS) sequentially, graphics cards exceed this performance by orders of magnitude due to their parallel-processing structure [39, 17]. Because of this, commercially available graphics cards can be used for accelerating the calculations that a holographic microscope requires.

Until recently, the graphics cards were only programmable by graphics APIs which are highly infeasible for general purpose calculations. Luckily, this has changed with the new programming models that are specifically designed for implementing a generic algorithm on graphics cards. This approach is also known as General Purpose computing on GPU (GPGPU) and it has proven to be very effective in other applications as well [16, 45]. Typically, the algorithm is developed in a parallel code structure that utilizes resources that are already available on the graphics card. OpenCL is the currently the most dominant open general-purpose GPU computing language. On the other side, the dominant proprietary framework is Nvidia's CUDA: Computed Unified Device Architecture.

3.2 Work-flow of GPU

Each physical processor contains essential processing units and storage facility such as an arithmetic logic unit, floating-point unit and a memory. The data stream is split up between processors and processed in parallel. The same kernel is executed on multiple processors of a GPU. Although each processor in a computational unit operates the same piece of code, they work independently. As a result, the outputs

of individual processors differ.

Each kernel function is executed on a grid of cores that consists of $m \times n$ processing blocks. The operation of every single processing block inside a grid is further divided into t number of threads and each thread is processed concurrently. The thread hierarchy allow scalability across different graphics cards with distinct processor count. Eventually, a virtually 3D computing structure with dimensions of $m \times n \times t$ is achieved where the kernel function is executed in every thread concurrently. An illustration of this computing architecture is shown in figure 3.1.

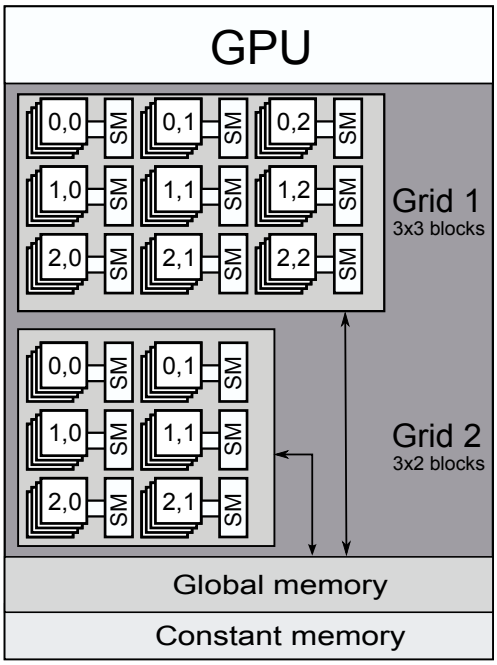

Figure 3.1: Generic architecture of an Nvidia GPU. SM states for shared memory.

The memory structure of a GPU has three layers: global memory, shared memory and registers. The communication between threads inside a single block is performed through shared memory (SM). At any given time, each thread in the block can access the same data in the shared memory with a very small latency. Therefore, shared memory must be utilized properly to obtain a better performance from the computational block. However, shared memories have relatively small capacity in

general. For example, NVidia GTX 660 Ti which used in experiments has compute capability 2.0; which means 48 Kbyte of shared memory per block. Therefore, it may not be adequate when the input data is large such as a complex wavefront data used in hologram reconstruction. For instance, to store and process a 1024×1024 pixels, single precision floating-point hologram image requires 32 megabytes of memory space and it can not fit in to the shared memory. In such conditions, global memory is used to store large data such as a hologram.

High volume communication between different blocks must be performed over the global memory. However, accessing the global memory of the graphics card can be a bit tricky. Any optimization in this aspect will affect the performance dramatically. Essentially, the order of accesses to the global memory has a direct impact on the performance. In order to use the GPU at full capacity, the access order for the global memory must be coalesced [46] such that consecutive threads in a block access to consecutive addresses in the global memory. Thus, the memory bandwidth is used at full capacity and minimum clock cycles are wasted due to blocking memory accesses. By this organization, for example, Nvidia Geforce GTX 660 Ti becomes able to read 32 consecutive memory addresses by one call.

Registers have the smallest latency. Therefore, one has to store as much as data in registers. However, the registers are only utilized at compile time. Otherwise, the data is stored in the thread-local part of the global memory, which again produces the same high latency [47].

The GPU kernels can be optimized by reducing the data latency, optimal access pattern to memory and optimal size of the thread blocks [47].

3.3 Timings

In experiments, we have used an Nvidia Geforce GTX 660 Ti for accelerating the reconstructions. This graphics card is one of the middle-class models which is manufactured for the gaming industry. The graphics card contains 1344 physical core processors and a 158.6 GB/s memory bandwidth. The detailed specifications of the Nvidia Geforce GTX 660 Ti is given in table 3.1.

	Nvidia Geforce GTX 660 Ti
Cores	1344
Memory	2 GB
Memory Int	192 bit
Memory BW	158.6 GB/sec
Clock speed	980 MHz
GFLOPS	1880 GFLOPS

Table 3.1: Hardware specifications of Geforce GTX 660 Ti

The reason for choosing an Nvidia card is the CUDA that is more mature than any other alternatives and supports many high-level functionalities. In addition, Nvidia distributes the proprietary libraries that were customized to work on Nvidia devices such as basic linear algebra libraries and various transform functions. For example, fast Fourier transform implementations of Nvidia (CUFFT) gives the best performance in the GPU market [46].

In order to compare the timings of CPU and GPU based approaches; each reconstruction method is implemented on MATLAB environment and CUDA environment. The test computer is equipped with an Intel Xeon W3670 processor and an Nvidia GTX660 Ti graphics cards.

The table 3.2 shows that utilizing the graphics card reduces the reconstruction time up to 100 times. A single reconstruction which takes almost a second with traditional processors is done in less than 10 ms. The speed-up in auto-focusing is

	Pre-calculations (ms)		Calculations (ms)		Total (ms)	
Reconstruction method	CPU	GPU	CPU	GPU	CPU	GPU
Fresnel approx.	787	4.8	150	4.4	937	9.2
Convolution	537	4.23	197	4.77	734	9
Angular Spect.	744	2.9	197	6.2	941	9.1

Table 3.2: Reconstruction times in millisecond for all methods

	CPU (Intel Xeon W3670)	GPU (NVidia GTX 660 Ti)	Speed-up
Reconstruction	941 ms	9.1 ms	103.4 ×
Auto-focusing	50 ms	5 ms	10 ×
Total	991 ms	14.1 ms	70.28 ×

Table 3.3: CPU versus GPU timings of Angular Spectrum method

relatively smaller, since smaller versions of the original hologram is used in auto-focusing. Smaller but multiple reconstructions reduce the efficiency of the graphics card. In any case, reconstruction and auto-focusing are performed at higher than video rates using the graphics cards as hardware accelerators.

4 DIGITAL HOLOGRAPHIC MICROSCOPE

A holographic microscope is set to be a better alternative to conventional light microscope. One important feature of a holographic microscope is the ability to capture the scene and do the focusing numerically on computers. Therefore, there is no need to do mechanical focusing alignments when recording the hologram. Moreover, focused images of particles that are separated on different focus planes can be obtained on demand.

Transparent objects do not alter the amplitude of the wave passing through. As a result, they are invisible under traditional microscopes and they should be stained before the imaging process. Moreover, staining can lead to plenty of unwanted results. For instance, staining kills biological cells and imaging them under a traditional microscope becomes impossible while they are still alive. However, images of transparent objects can be captured without staining with a digital holographic microscope. Although the transparent object is invisible in the intensity image, it is clearly visible in the phase image of the reconstruction. This is because the transparent objects apply a certain phase delay to the wave passing through. As a result, live biological cells can be imaged without staining with a digital holographic microscope.

4.1 Operational Flow of the Microscope

The operation cycle of the DHM consists of four steps which are called hologram acquisition, pre-processing, auto-focusing and reconstruction. In the hologram acquisition step, three holograms of the specimen are recorded and transfered to the

graphics card's global memory. The remaining steps are performed on the GPU via proper kernel functions. The holograms that have been recorded with different reference phases are combined as in equation (2.6) to obtain the far field of the object wave. This step consists of point-wise matrix operations and it is described in algorithm 1.

Algorithm 1: Phase-shifting holography method
Input: Three holograms I_0, $I_{\frac{\pi}{2}}$ and I_π with phase shift applied to the reference waves
Output: The hologram of only the object image $O(x, y)$

1. Copy holograms to the global memory of GPU.
2. Compute real part of $|O(x, y)| = \frac{1}{4}(I_0 - I_\pi)$.
3. Compute imaginary part as $\frac{1}{4}(2I_{\pi/2} - I_\pi - I_0)$.
4. Calculate intensity and phase components of $O(x, y)$.

Later, the far field of the object wave is scaled down four times for speeding up auto-focusing [40]. The scaled hologram is reconstructed over an interval with a reasonable step size and the focus distance of the specimen is estimated as in algorithm (2). For example, if a 2 cm interval is to be analyzed with 1 mm step-size, 20 different reconstructions are performed in total. Afterwards, every reconstruction is subjected to sharpness evaluation by equation (2.23) and the distance which gives the highest sharpness value is selected as the true focus distance (Algorithm 2).

Algorithm 2: Focus distance estimation
Input: Hologram O(x,y) of specimen, scaling coefficient s, distance interval $d_s - d_f$ and step size Δd
Output: Focus distance d_{focus} of the object

1. Scale $O(x, y)$ with scaling ratio s.
2. Compute the scaled reconstruction $R_s(x, y)$ at distance d_s using algorithm 3.
3. Calculate the quality of $R_s(x, y)$ using a sharpness function.
4. Increment d_s by Δd.
5. Repeat from step 2, until $d_s = d_f$.
6. Select d_{focus} that produces the highest quality scaled reconstruction.

Later, the full-sized object field is reconstructed at the previously estimated focus distance. The reconstruction procedure is shown by the algorithm 3 where all fast Fourier transforms are calculated with the CUFFT library that is provided by Nvidia.

Finally, the reconstruction of the original sized hologram is displayed on the screen as a 3D surface by using the phase image for the height-map and intensity image for the colour-map of the surface. The overall flow of the algorithms are illustrated in figure 4.1.

Note that, whole computation is performed on the graphics card by utilizing it's parallel structure. Thus, the computation time is reduced such that; both auto-focusing and hologram reconstruction can be performed at higher than the video rates. Moreover, the microscope operator does not need to do manual focusing. Focused 3-D image of the specimen is displayed automatically.

Algorithm 3: Hologram reconstruction using angular spectrum method
Input: Hologram O(x,y) of specimen and reconstruction distance d
Output: Reconstructed complex image $R(x, y)$

1. Calculate $F_o = FFT[O(x, y)]$ using $CUFFT$.
2. Compute 2048×2048 impulse response $T_d(x, y)$.
3. Compute $T_f(x, y)$ by multiplying $T(x, y)$ with F_O.
4. Calculate $R(x, y) = IFFT[T_f(x, y)]$ using $CUIFFT$.

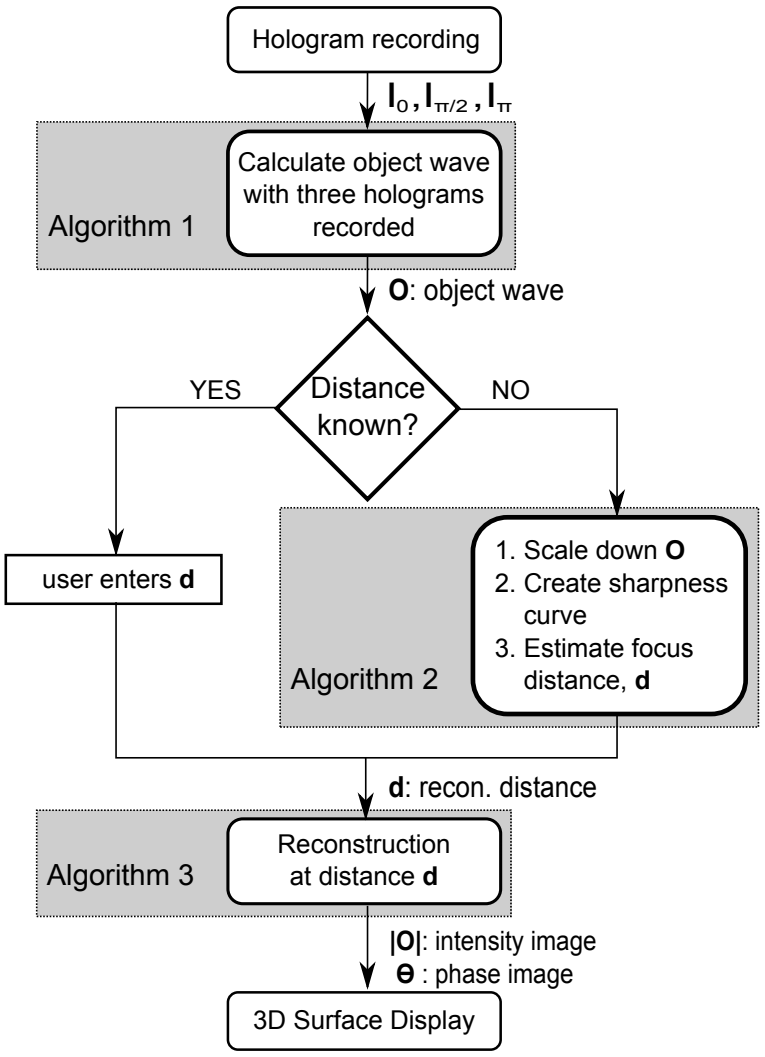

Figure 4.1: Flow of operations in an auto-focusing DHM.

4.2 Digital Holographic Microscope Set-up

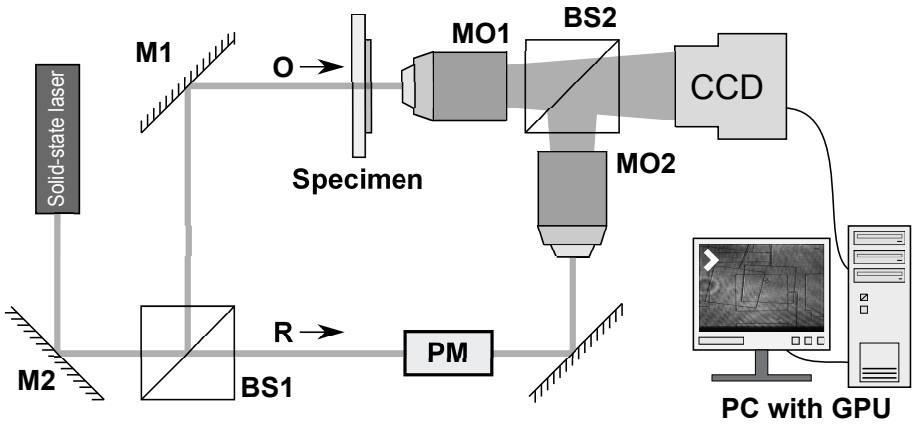

Figure 4.2: The transmission based DHM setup. The laser beam is divided into two arms by the beam splitter BS1. The reference wave is modulated by a phase modulator (PM) and the object wave is transmitted through the specimen. Before joining the two arms of the interferometer by the second beam splitter BS2, object image is magnified by the microscope objective MO1. In order to compensate the wave front curvature caused by the MO1, an identical microscope objective MO2 is placed on the reference path. Finally, interference of the two beams is recorded by a CCD camera.

The digital holographic microscope we built consists of a Mach-Zehnder interferometer with an opto-electronic phase modulator placed in the reference arm. The schematic of the microscope is given in figure 4.4. A 5 mW solid state laser with wavelength 672 nm is used as the laser source. The beam-splitter BS1 splits the linearly polarized laser beam into object arm and reference arm. The specimen is placed in the object arm and the laser is transmitted through. The emergent object field is magnified by a 10x (NA 0.25) microscope objective. An identical microscope objective MO2 is also symmetrically placed into the reference arm in order to match the curvatures of the reference and object waves. The Newport 4002 broadband opto-electronic phase modulator is used to modulate the phase of the reference wave. Finally, a second beam-splitter BS2 joins the modulated reference wave and the object wave together and it forms the hologram in front of the monochromatic CCD. The camera used in the setup is a Sony S800 which has 1024×1024 pixels with pixel

dimensions of $3.75\mu m \times 3.75\mu m$. The specifications of the microscope are given in table 4.1. The figure 4.4 shows the schematic of the microscope where dotted lines represent the laser beam. In addition, four other photos of the microscope can be seen in figure 4.3.

Table 4.1: Specifications of the DHM

DHM feature	Specification
Mode	Transmission
Wavelength (λ)	672 nm (Solid State)
Filtering	Spatial or Phase-shifting
Capture rate	5 holograms per second
Hologram size	1024×1024
CCD pixel dimensions	3.75μm $\times 3.75\mu$m
Lateral resolution	2.2 μm
Field of view	320 μm $\times 320\mu$m
Magnification	≈ 12

4.3 Control Interface of the Microscope

A software has been developed to control the digital holographic microscope. The software operates the camera, the phase-modulator and the graphics card in accord to provide a transparent microscope experience. At each cycle, the software captures three holograms with certain phase shifts in the reference arm. The amount of phase-shift is provided by user during the device calibration. After capturing three holograms with different phase shifts, the holograms are transfered to graphics card's memory.

Whole computation is performed in GPU. First, three holograms are processed to filter the extraneous images using phase-shifting technique. Then, the software reconstructs the filtered object image at the given distance. All three reconstruction methods (Fresnel's method, convolution method and angular spectrum method) are

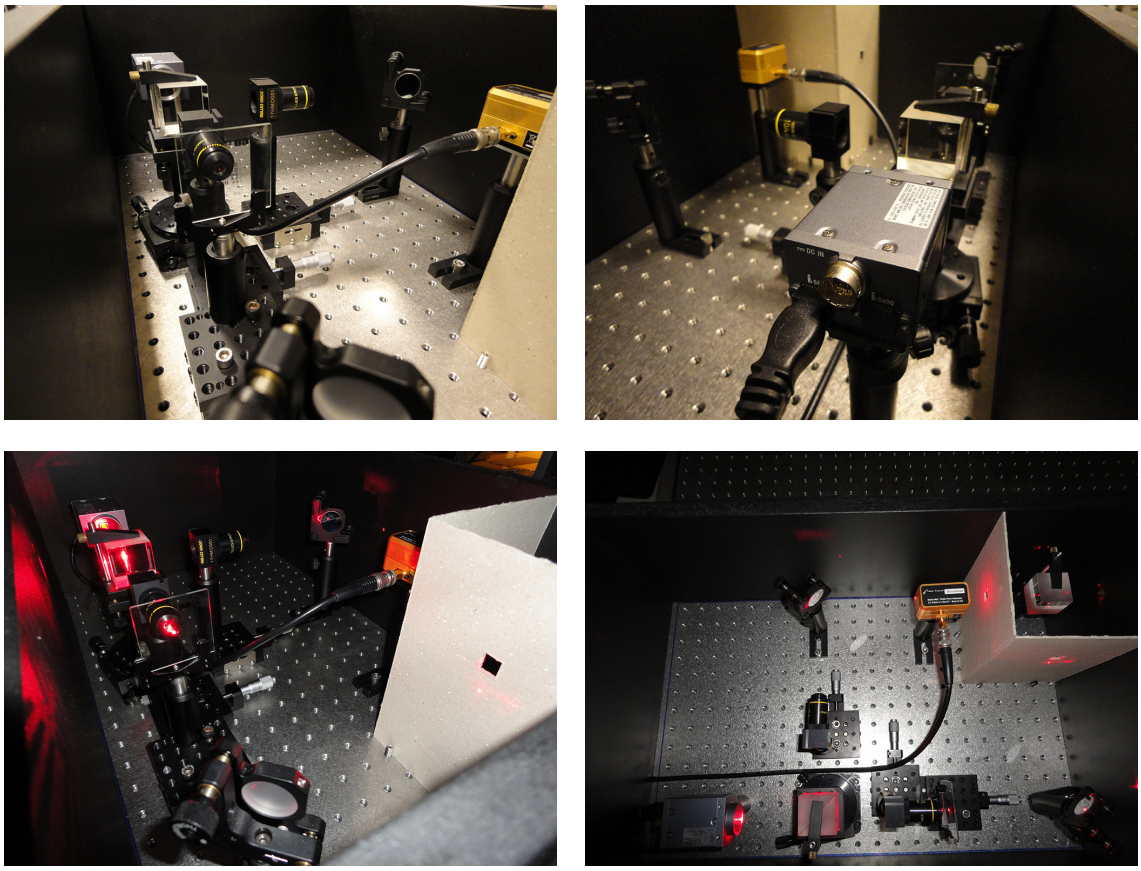

Figure 4.3: The figure shows four photos of the digital holographic microscope.

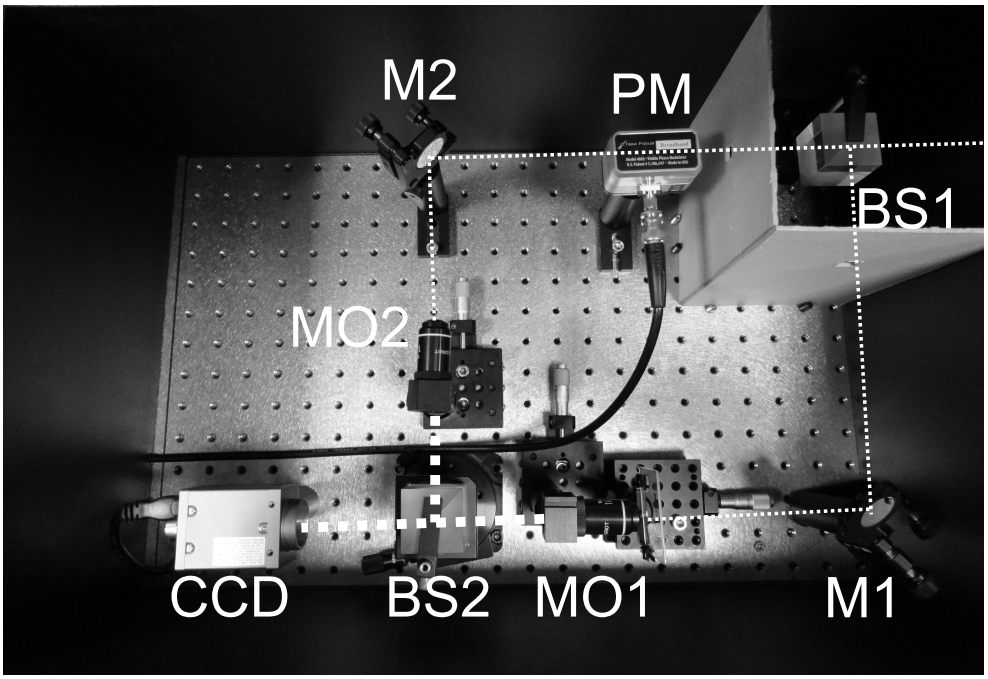

Figure 4.4: Picture of the digital holographic microscope. All equipments including the camera are sealed in a wooden box on an optics table. The optics table isolates the vibrations and the wooden box prevents air flow which distorts hologram recording.

supported by the software, and the reconstruction method can be changed at any time.

A screen-shot of the software is shown in figure 4.5. On the upper part of the view, the hologram video stream is displayed. This part is updated in real-time depending on the capture rate of the camera. On the bottom side, all the control buttons and sliders are placed. For instance, the reconstruction distance can be set manually using a slider and the reconstructed image appears in the 3D view instantly. 3D view window as shown in figure 4.6 displays the reconstructed image by using the phase image for the height-map and intensity image for the colour-map of the surface. The user can change the orientation of the reconstruction using mouse and adjust the zoom level with the mouse wheel. Surface plotting is implemented using the OpenGL library. The software uses the OpenGL and CUDA interoperability services to transfer reconstructed image to the frame buffer of the display system [48].

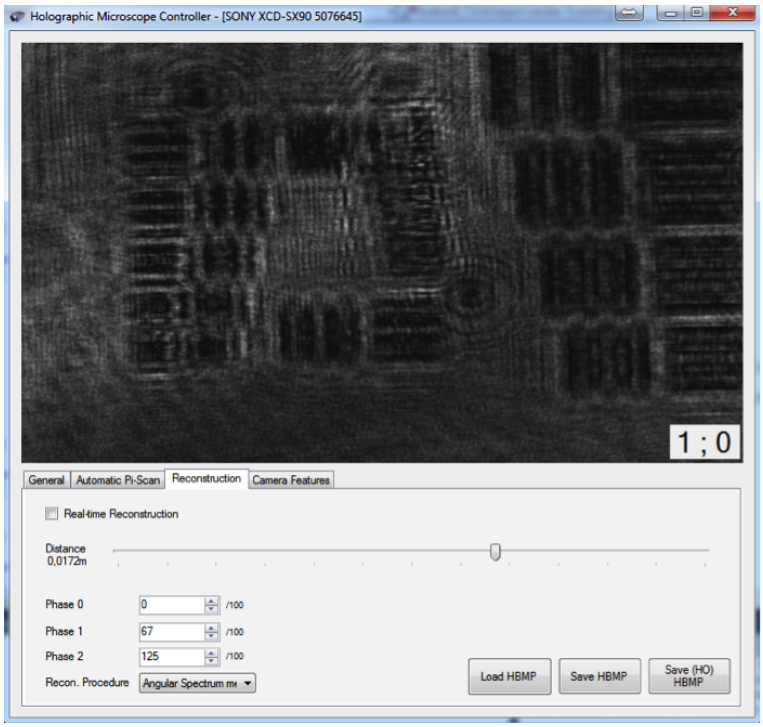

Figure 4.5: Reconstruction view.

Therefore, no extra time is wasted for transferring the data back to the host memory. The reconstructed image is display in 3D using OpenGL's vertex buffer object.

4.4 Experiments

The microscope is calibrated with a high resolution USAF Chart. The magnification rate of the microscope is measured as 12×; yet, the exact rate depends on the position of the sample. When the sample is moved away from the microscope objective, the magnification slightly increases. With our microscope, we are able to observe the element 6 of group 8 of the calibration chart, which corresponds to capturing 456 line pairs per millimeter. Hence, the lateral resolution is estimated as $2.2\mu m$ in both axises and the field of view is $320\mu m \times 320\mu m$.

We have analyzed several magnitude and phase objects under the DHM. The experiments have been performed on three different types of samples which are given

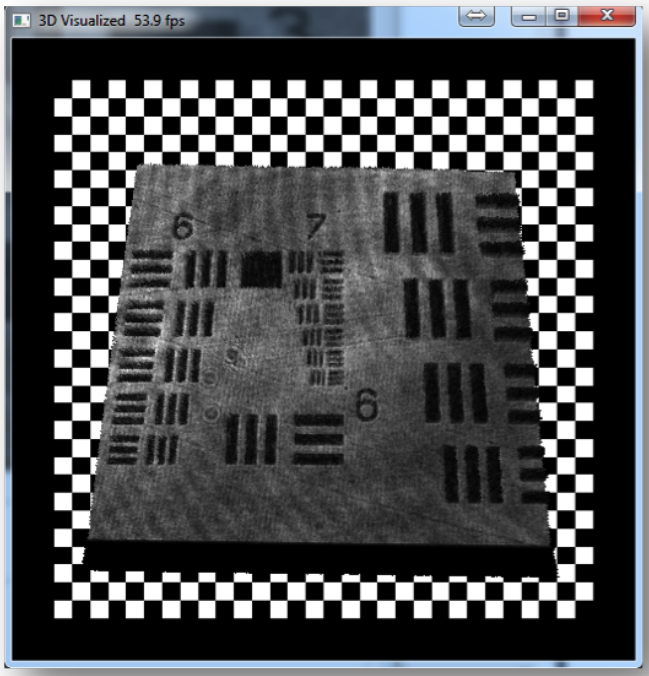

Figure 4.6: Real-time 3D surface plot of the specimen.

in figure 4.7. The first sample is the hologram of human epithelial cells. Similar to conventional light microscopy, the cells in figure 4.7-a are not visible in the intensity image when the image is exactly focused. However, those cells can be resolved in the phase image of the reconstructed hologram where the gray-levels represent the thickness of the specimen.

A similar scenario is observed in the second sample, where the test object is prepared by coating $2\mu m$-thick photo-resist material (AZ 5214E) onto a microscope slide. In this sample, the edges are more visible in the magnitude image because the structure has steep edges. However, the phase image still supplies more structural information about the object. For example, the quality of the coating can be examined by analyzing the corresponding regions of the phase image. The last sample in figures (4.7-e, 4.7-f) is the hologram of the 1951 USAF resolution chart. The reso-

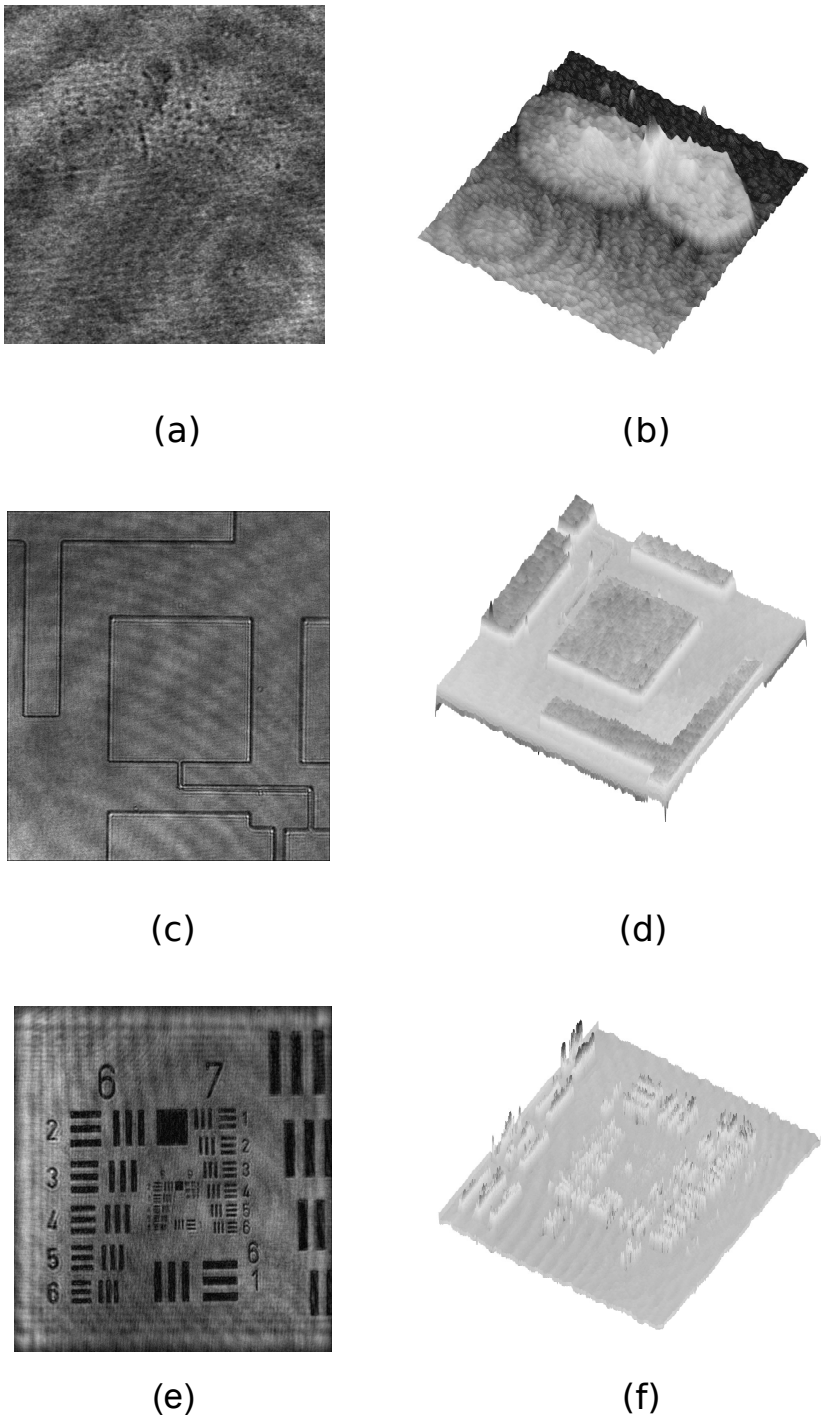

Figure 4.7: The figure shows the intensity images (a, c, e) and the phase images (b, d, f) of human epithelial cells, photo-resist test sample and USAF calibration chart.

lution chart acts like a binary mask for the object wave and it only modulates the magnitude of the passing light. Therefore, the phase part of the reconstruction (4.7 f) does not contain any thickness data and the 3D reconstruction is not meaningful.

4.4.1 Comparing the reconstruction methods

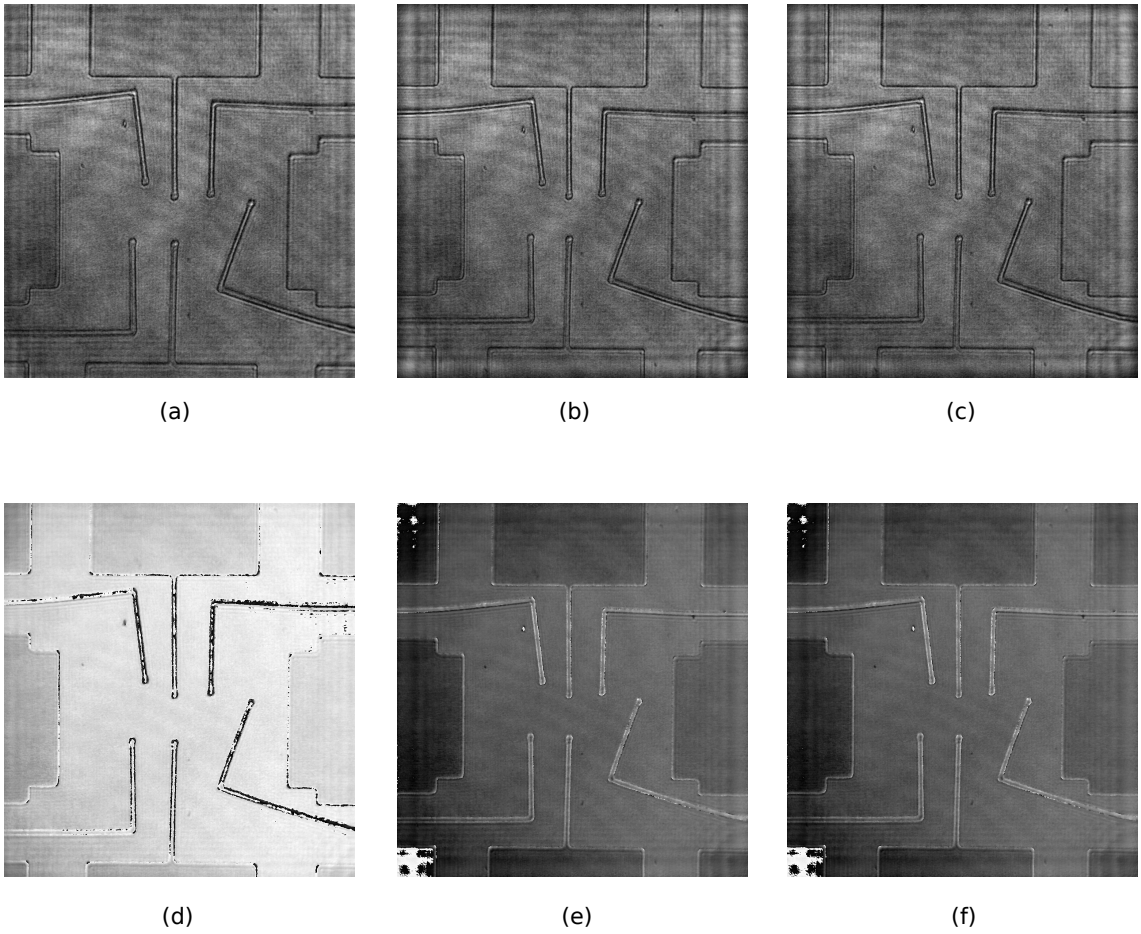

Figure 4.8: Figure shows amplitude and phase images obtained by three of the methods mentioned previously. (a, b, c) are the amplitude images and (d, e, f) are the phase images calculated with Fresnel method, convolution method and angular spectrum method.

Another part of the photo-resist hologram is used for comparing the reconstruction methods. The actual focus distance of the hologram is around 4 cm. The figure 4.8 shows the focused reconstructions obtained by the Fresnel method, convo-

lution method and angular spectrum method. The difference in the pixel dimensions is visible between Fresnel method and others such that (4.8.a) is slightly magnified compared to (4.8.b) and (4.8.c). Figure (4.9) shows another hologram recorded at $1cm$. Although, the Fresnel method and the convolution method are not working on that range, the angular spectrum method gives feasible results.

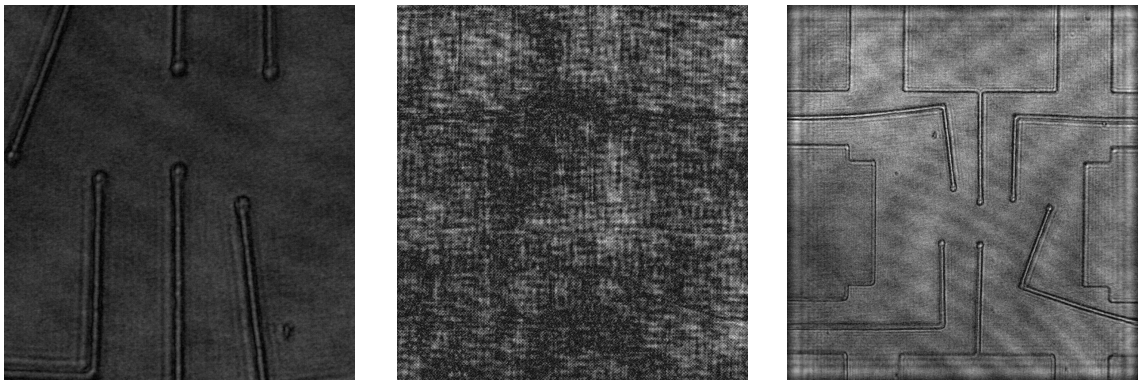

Figure 4.9: The figure shows the absolute image of three reconstruction: (a) Fresnel approximation method, (b) convolution method and (c) angular spectrum method. The reconstruction distance is $1mm$ and only the angular spectrum method works properly.

Figure 4.10 shows the reconstruction of USAF resolution test target, where reconstruction distance is 10 cm. In the figure, each column shows the reconstruction of a different method. The first and the third columns show the reconstruction of angular spectrum method and convolution method respectively. The center column shows the reconstruction of Fresnel's method. The hologram satisfies distance limitations of all methods and each method produces proper results. Especially, there is visually negligible difference between angular spectrum method and the convolution method. Since the reconstruction distance is much greater than the object dimensions, pixel dimensions of the Fresnel's reconstruction increases. As a results, the resolution of Fresnel's reconstruction degrades.

Figure 4.11 shows the reconstruction of human epithelial cell hologram whose

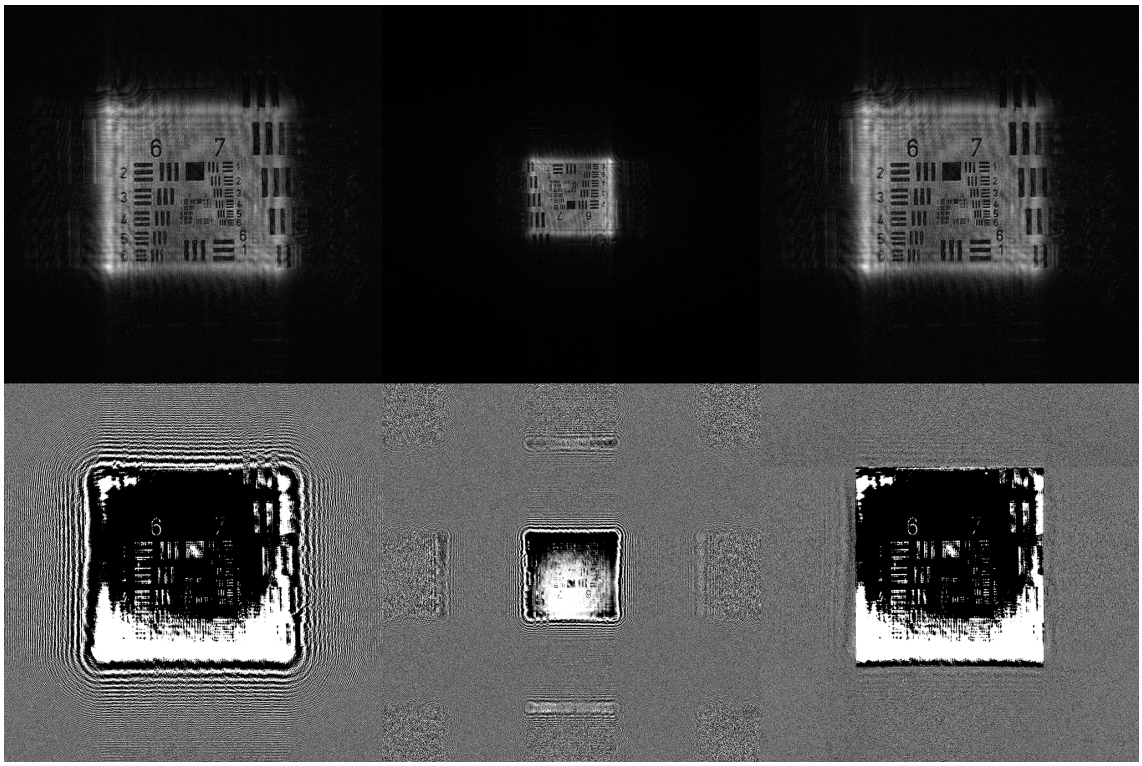

Figure 4.10: Figure show the reconstructions of USAF resolution test target's hologram. (a, b, c) are the amplitude images and (d, e, f) are the phase images calculated with angular spectrum method, Fresnel method and convolution method respectively.

reconstruction distance is 3 mm. The figure is organized as figure 4.11, where columns show reconstructions of angular spectrum method, Fresnel's method and convolution method respectively. Although, the hologram satisfies distance limitations of the convolution method, the distance constraint of the Fresnel is violated. As a results, the Fresnel's method produces erroneous result. However, the angular spectrum method and the convolution method produces proper reconstructions. In addition, this experiment reinforces the advantage of using a digital holographic microscope for imaging transparent specimen. Since epithelial cells are transparent objects, the cell image disappears from the amplitude image when the reconstruction is at focus. However, the cell applies phase shifts to the object beam, thus the cell is visible in the phase image.

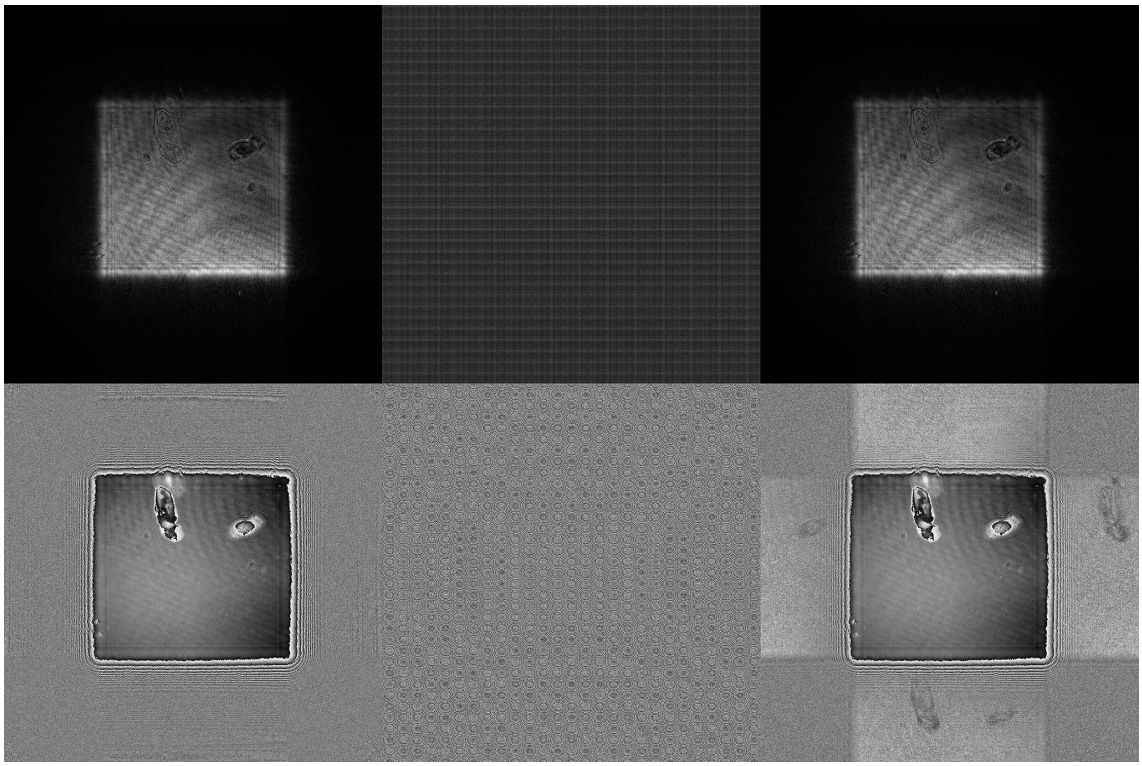

Figure 4.11: Figure show the reconstructions of human epithelial cell hologram. (a, b, c) are the amplitude images and (d, e, f) are the phase images calculated with angular spectrum method, Fresnel method and convolution method respectively.

4.4.2 Measuring the surface roughness

In traditional ways, one has to do plenty of measurements at different points from the surface of a material to obtain an overall measure of surface roughness. For example, atomic force microscopy and Rutherford backscattering spectroscopy can be used to measure the surface roughness [49]. This increases the error margin and requires huge effort compared the holographic method. The most significant advantage of measuring the surface roughness via holographic means is that the property at any position can be calculated by a single hologram.

In this experiment, surface roughness of a photo-resist(AZ 5214E) test structure was measured using a single hologram. For using in the experiment, a thin layer of photo-resist structure was developed on a microscope slide and the hologram of the structure was recorded. Then, the hologram is reconstructed at the true focus distance. Although the photo-resist is mostly a transparent object, the 3D structure of the coating is clearly visible in the phase image in figure 4.12.

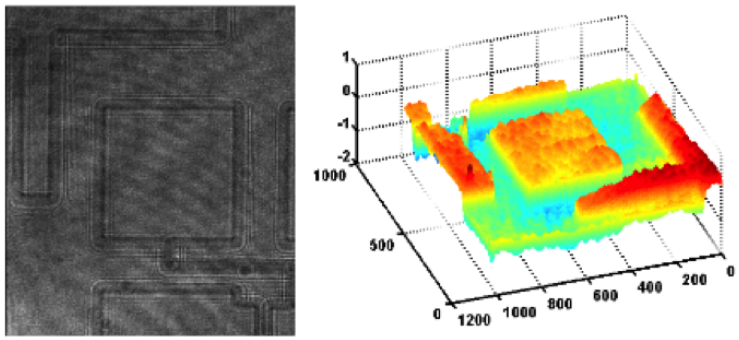

Figure 4.12: The image on the left is the photo-resist hologram. The image on the right is the reconstruction of the photo-resist hologram.

In order to measure the roughness of the photo-resist coating, a linear cross section of the center square block of the structure is extracted. Finally, mean square error of the one dimensional cross section is calculated (Fig. 4.13). In this specific example, the surface roughness of the coating is measured as 48 nm.

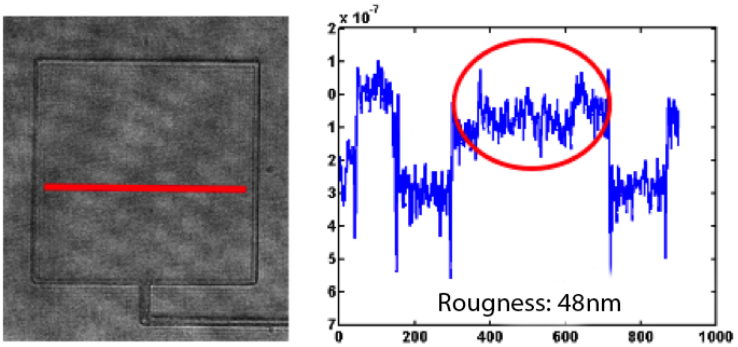

Figure 4.13: The image on the left is the amplitude image of photo-resist reconstruction. The image on the right is the cross section of the phase image of the photo-resist structure.

5 INCORPORATING AN OPTICAL TWEEZER TO THE DHM

It was already demonstrated 45 years ago that, a tightly focused laser light changes the momentum of small particles in general [31]. This change in momentum results in a pico-newton force on the particle which is used for trapping and manipulation. This phenomenon enables the researchers to develop a so called optical tweezer (OT) systems. Recently, optical tweezers become so popular especially in bio-science studies where they are used for trapping and manipulation of various types of specimen under a microscope.

This chapter provides an overview of basic optical tweezer principles and concepts of manipulation of particles under the microscope. Then, a real-time digital holographic microscope which includes an optical tweezer is introduced and the experimental results are presented.

5.1 Incorporating the Optical Tweezer

Figure 5.1 shows the setup of the digital holographic microscope with the optical tweezer. In order to reduce the effects of the gravity on the specimen, the microscope is built in vertical alignment as opposed to the previous version. A photograph of the setup is shown in figure 5.2 where a Mach-Zehnder interferometer is built for capturing transmission mode in-line holograms. A green (555 nm) laser is used in hologram recording. The beam-splitter BS1 splits the laser light into the object arm and the reference arm.

A 5mW red (672 nm) solid state laser is used for the optical tweezer beam. The

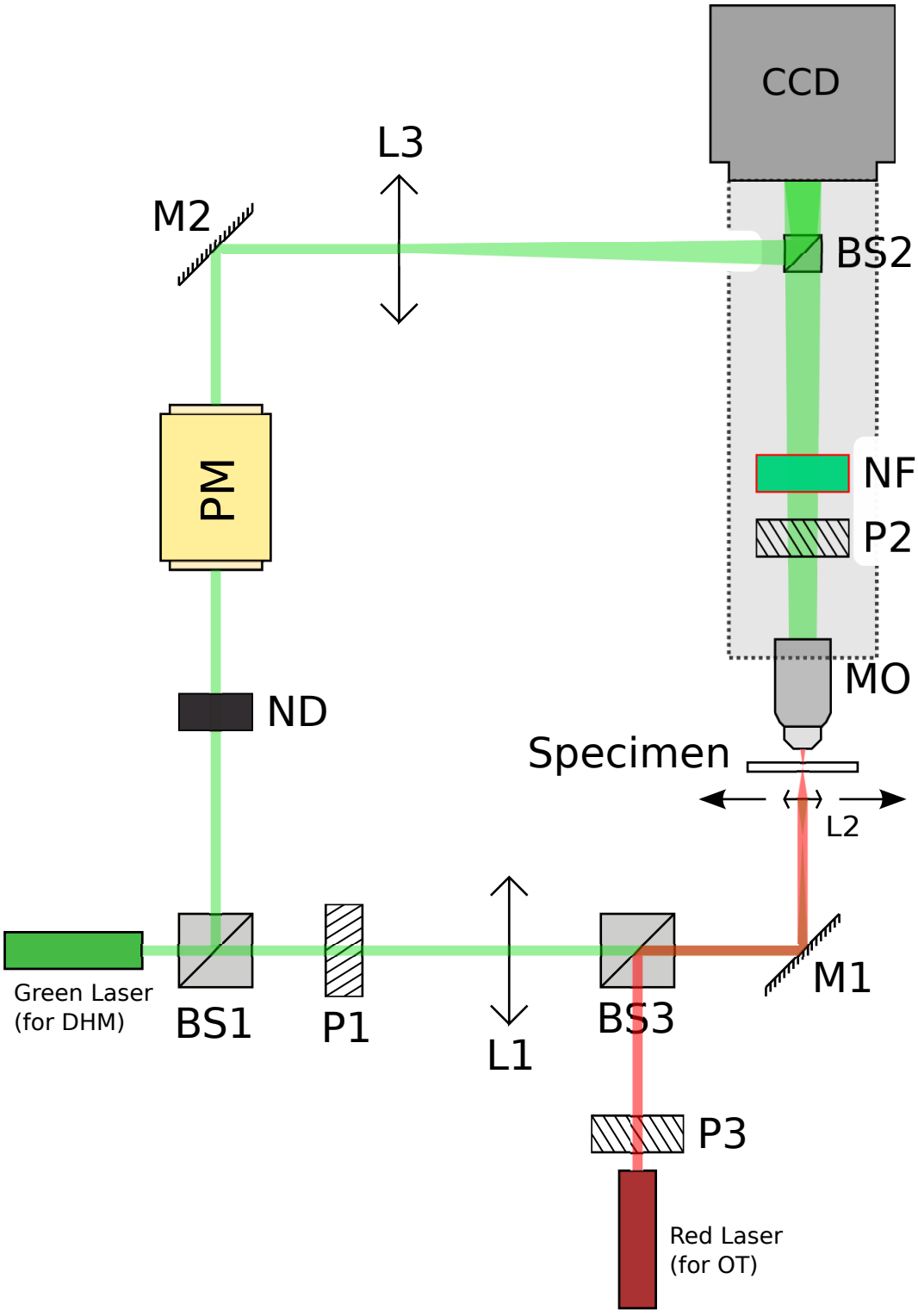

Figure 5.1: The digital holographic microscope with optical tweezer setup

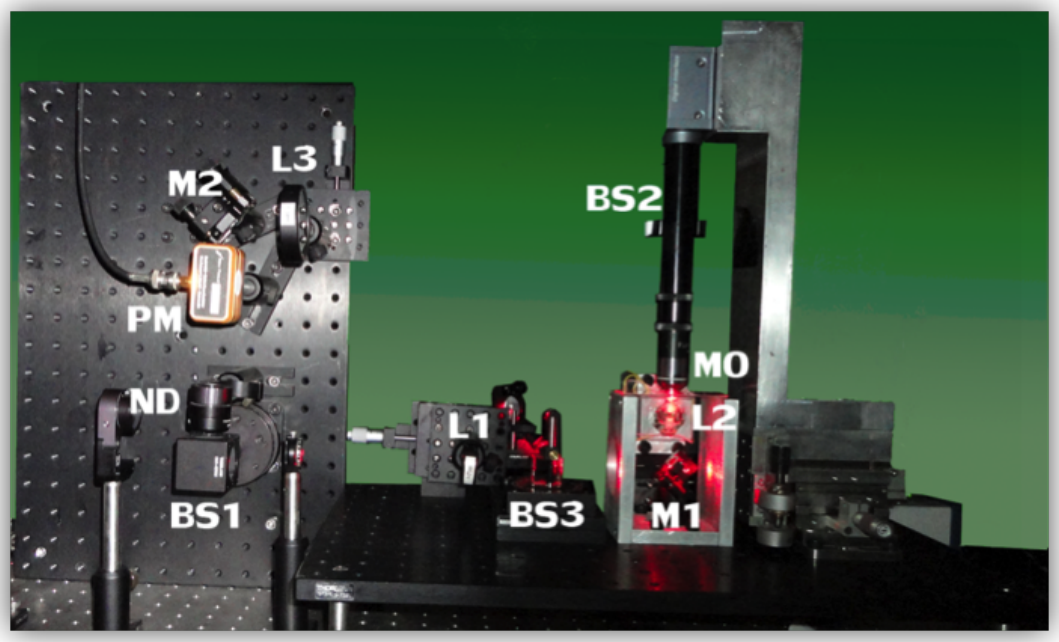

Figure 5.2: The photograph of the digital holographic microscope with the optical tweezer.

tweezer light joins to the optical path by the beam-splitter BS3 and it is reflected onto the sample by the mirror M2. The figure 5.3 shows the miniature coil-magnet assembly which is used for steering the tweezer beam. In contrast to the existing optical tweezer systems, ours steers a single free space lens which focuses the laser beam on the sample plane.

The miniature coil-magnet assembly is obtained by modifying a standard CD-ROM optical pick-up head. It is well known that, in optical tweezer experiments higher numerical aperture lenses are always desirable. Therefore, the lens on the original CD-ROM is replaced by an aspheric lens L2 with 4.5mm focal length and 0.55NA.

The coil-magnet assembly contains two sets of magnets which are perpendicular to each other. Also, the magnets are wrapped with coils in order provide movement to the coil assembly. The two analog output ports of the National Instrument USB

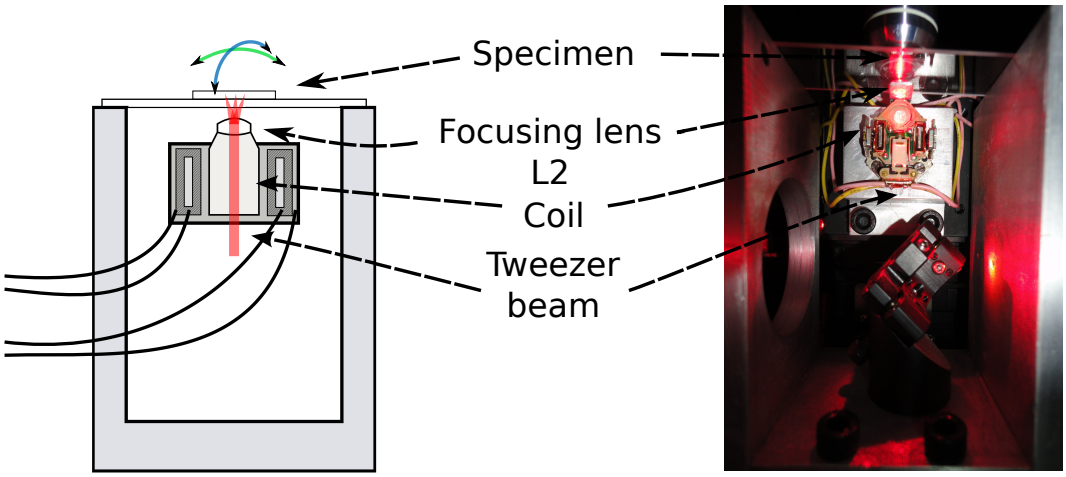

Figure 5.3: The figure shows the apparatus for steering the tweezer beam.

6251 DAQ is connected to the coils to achieve computer controlled movement of the tweezer beam.

When a current is applied, a magnetic force is created on the coil assembly in the direction perpendicular to the plane defined by the magnetic field and the current flow. This force changes the rotation of the coils assembly which steers the tweezer beam over the sample surface. In order to move the lens from edge to edge in the field of view of the imaging area, the coils require approximately 6mA for both axes. This current level corresponds to a rather low voltage drive which increases the noise in the system. Therefore, in order to increase the resolution of the movement, series resistances are added to increase the driving voltage for a given displacement.

Unfortunately, the focusing lens of the tweezer beam L2 also refracts the green laser which is used in hologram recording. In order to compensate the effect of the L2 on the green laser light, a thin lens with 175mm focal length is placed on the object path. The focal points of the L1 and the L2 are super-positioned, hence together they act as a beam reducer. As a result, the collimation of the green laser is preserved as shows in figure 5.4.

The green laser passes through the specimen and the emergent wavefront is mag-

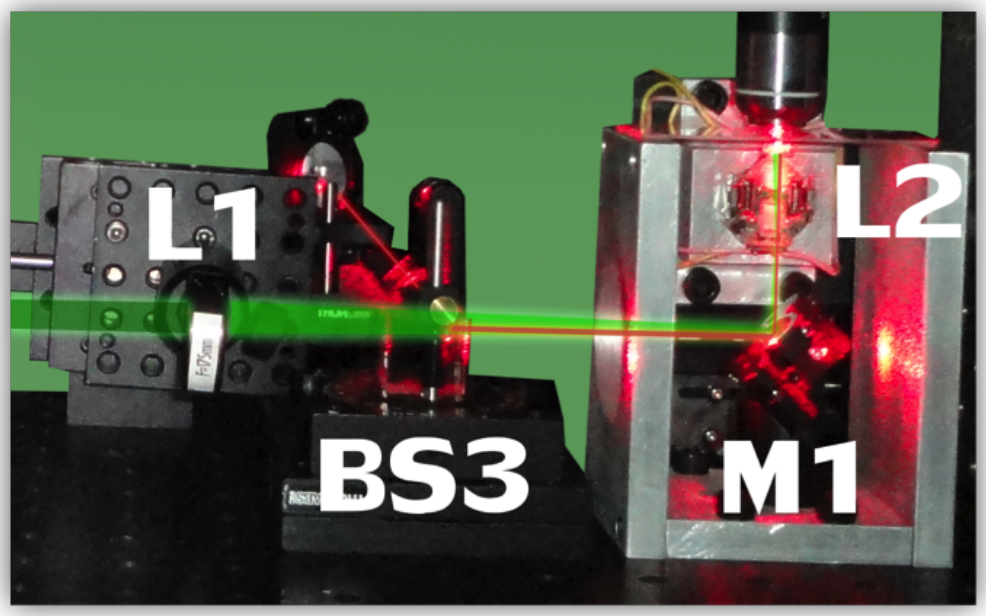

Figure 5.4: A close-up view of beam reducer.

nified using a 100x DIN microscope objective. A 1cm wide beam-splitter BS2 is placed inside the aluminum DIN tube adapter which connects the the microscope objective to the CCD camera. The expanding object wave and the reference wave are combined by the BS2, and an interference pattern is formed over the CCD's sensor.

It is essential to block the tweezer light to reach the CCD sensor since it has much more power than the interference pattern. Otherwise, the tweezer light saturates the pixels of the CCD and the hologram can not be captured properly. P2 and P1 polarizers are places in perpendicular to stop the tweezer light before reaching the camera. However, using only the polarizers is not adequate since the tweezer light still saturates most of the CCD pixels. To overcome this issue, a red notch filter is placed after the microscope objective. The polarizer P1 and the neutral density filter ND are incorporated in the setup to adjust the contrast of the interference pattern.

The Newport 4002 broadband opto-electronic phase modulator is placed on the

reference arm in order to record phase shifted holograms. Previously, the phase modulator was controlled by one of the two analog output ports of the National Instrument USB 6251 DAQ. Since those two analog ports are used for steering the tweezer beam, the circuit in figure 5.5 is built for generating the desired analog voltages from the two bit digital inputs. The potentiometer is used for adjusting the analog voltage level V which is fed to a voltage divider. By altering the input pins, the output voltage can be set to 0, $V/2$ or V which corresponds to 0, $\pi/2$ and π degrees of phase shifts respectively.

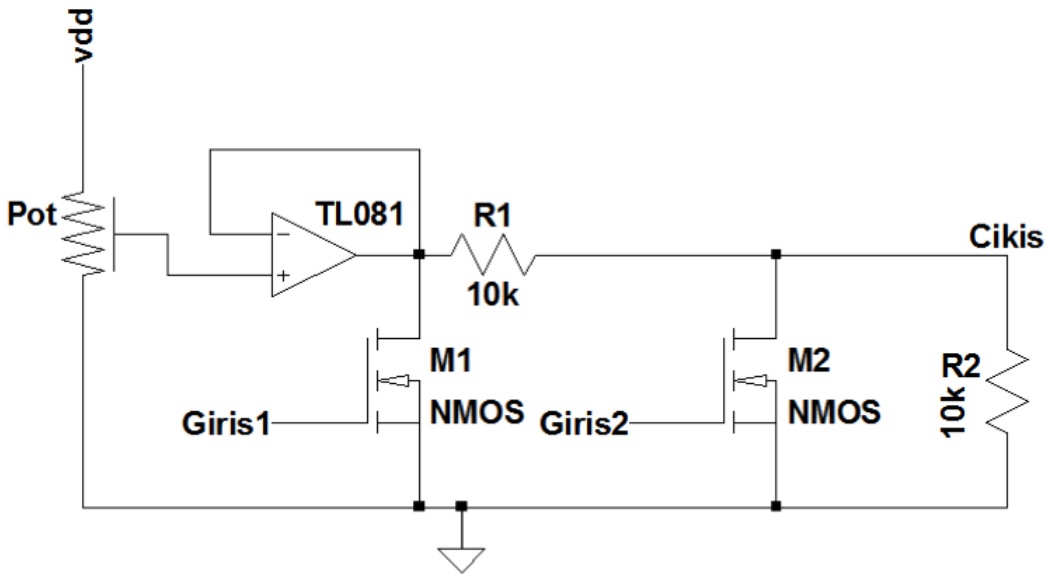

Figure 5.5: The circuit for driving the phase sifter with two digital inputs.

The table 5.1 shows the specifications of the digital holographic microscope with the optical tweezer. Moreover, two photographs of the device can be seen in figure 5.6, and the figure 5.7 show the overall diagram of the electronic system used in the microscope.

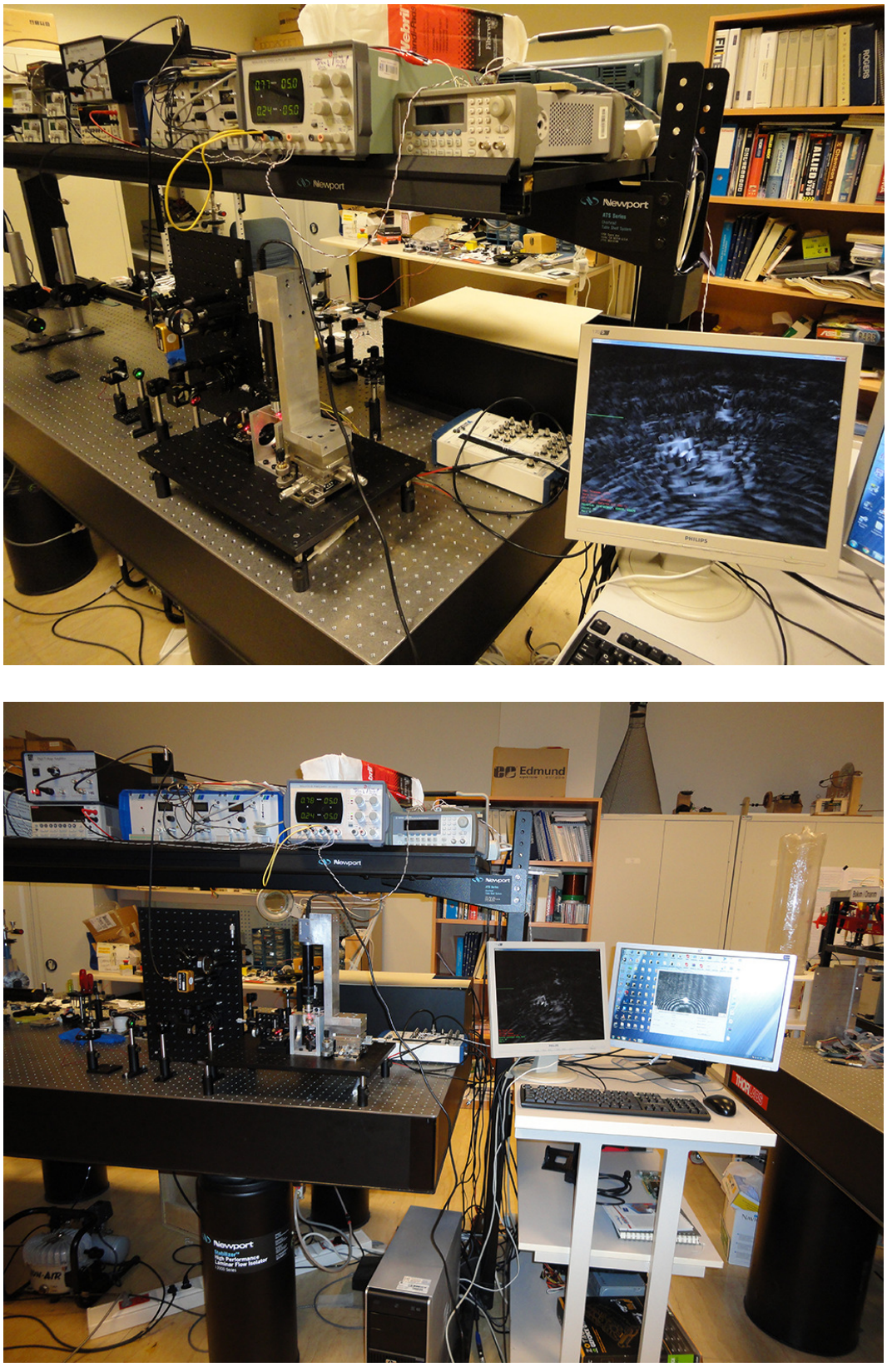

Figure 5.6: The photographs of the microscope.

Table 5.1: Specifications of the DHM with Optical Tweezer

DHM feature	Specification
Mode	Transmission
Wavelength	555 nm (Solid State)
Tweezer Wavelength	672 nm (Solid State)
Filtering	Spatial or Phase-shifting
Capture rate	5 holograms per second
Hologram size	1024×1024
CCD pixel dimensions	3.75μm $\times 3.75\mu$m
Field of view	30 μm $\times 30\mu$m
Magnification	≈ 110

5.2 Software Development

The software was improved to enable holographic imaging and optical tweezing simultaneously. Figure 5.8 shows the control view that is developed to operate the optical tweezer. There are two perpendicular sliders for steering the tweezer beam on the surface of the sample plane. In addition to the sliders, the position of the trap can be set by clicking on a point on the hologram. Calibration is required in order to estimate the currents for moving the trap to the actual location which corresponds to the click location. The calibration is done using the two-axis sliders. First, the tweezer trap is moved to the four corners of the imaging view and the currents for moving the trap to each corner are recorded. Later, those four sets of current levels are used to calculate the current required to move the trap to any point inside the imaging view.

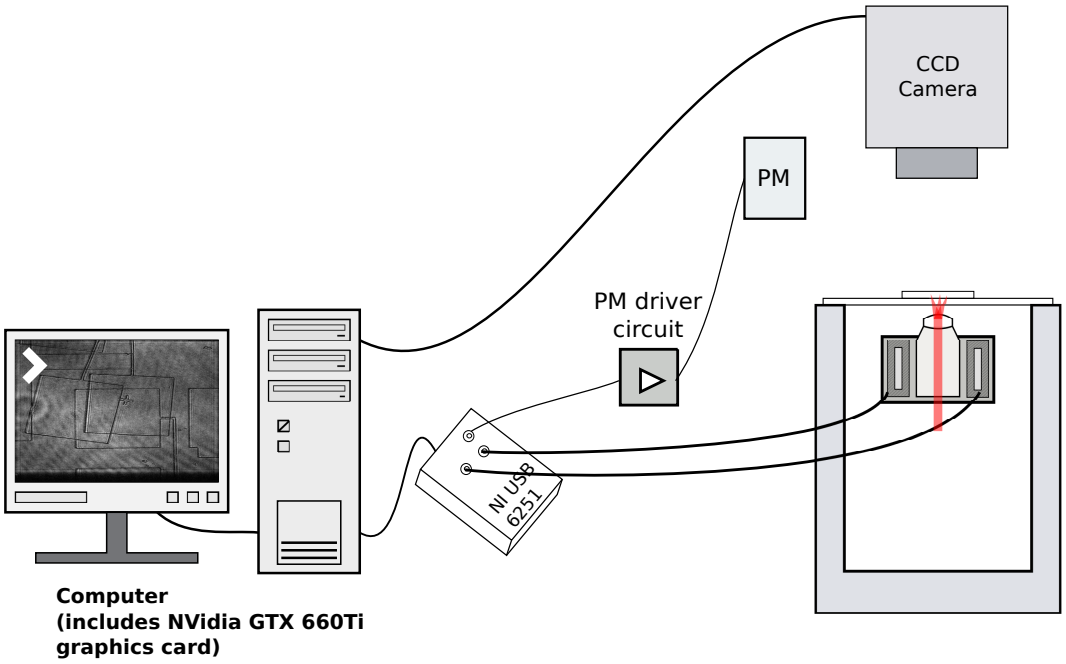

Figure 5.7: The diagram of the electronic equipments used in the microscope.

5.3 Experiments

5.3.1 Holographic Imaging

As opposed to the previous microscope, a 100x objective is used rather than a 10x objective. Therefore, approximately ten times smaller particles can be observed with the microscope. The microscope objective is only placed on the object path, as a result the object wave and the reference wave curvatures are not matched. Therefore, a circular interference pattern is obtained as shown in figure 5.8. The interference pattern has small fringes and this complicates the phase-sifting filtering method since even a tiny deviation in the control signal of the phase modulator causes significant error. Unfortunately, those errors appear in most of the holograms which are recorded with this microscope. The intensity images always carry the ghost image of the interference pattern as shown in figure 5.9. Moreover, due to the curvature mismatch, the phase image of the reconstructions contains multiple wraps, which precludes

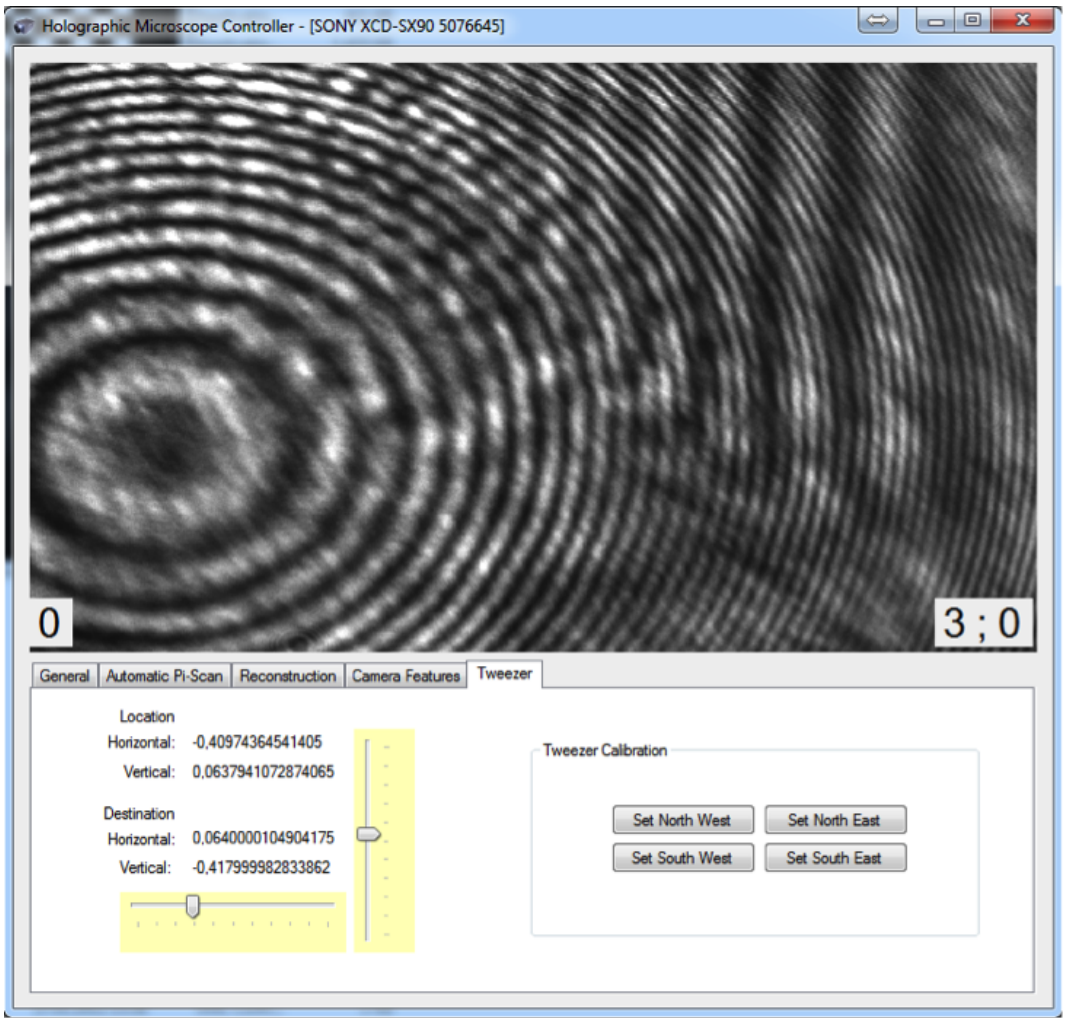

Figure 5.8: The software view for controlling the optical tweezer.

analysis of the phase image.

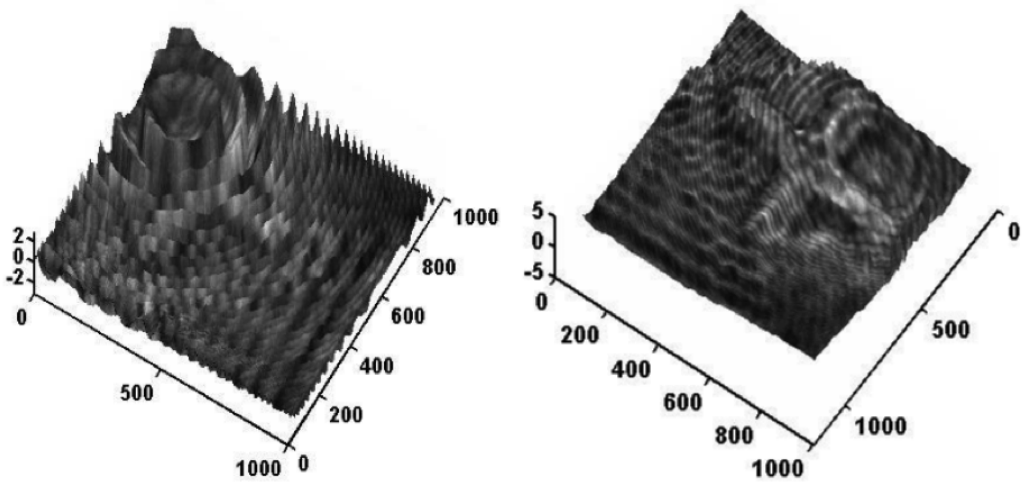

Figure 5.9: The figure shows two reconstructions (a) without reference correction, (b) with reference correction.

The figure 5.9 shows two intensity images of the photo-resist hologram reconstructions. The reference wave in hologram recording is a spherical wave, thus the reconstruction must be done with a wave that has identical properties. In order to examine the effects of reconstructing with a wrong reference wave, the hologram is reconstructed with a plane reference wave.

In figure 5.9, a reconstruction is performed with a planar reference wave and since this reference wave is different than the reference wave used in the recording, plenty of wraps appear in the phase image such that phase-unwrapping algorithm must be used to unwrap the phase. However the unwrapping does not provide the original phase map, so it is essential to use a spherical reference wave as shown in figure 5.9-b. It is clearly seen that the curvature of the phase image surface is corrected and the phase wraps in are disappeared.

The figure 5.10 shows the reconstruction of five yeast cells hologram with 1.2cm focal length. The image on the left is the intensity image and the image on the middle

is the phase image of the reconstruction at the actual focus distance. The image on the right shows the 3D reconstruction of the surface by using the phase image for the height-map and intensity image for the colour-map of the surface.

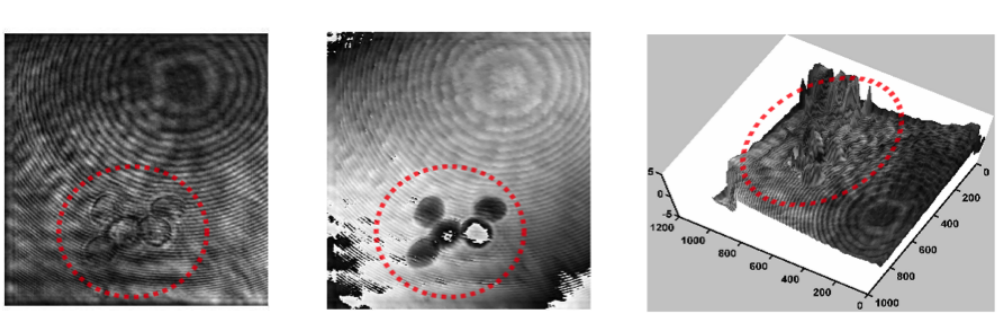

Figure 5.10: The figure shows the reconstruction of the five yeast cells hologram with 1.2cm focal length. (a) is the intensity image, (b) is the phase image and (c) is the 3-D surface plot of the reconstruction.

The figure 5.14 shows reconstructions of various holograms and their reconstructions. Each row contains the hologram and the reconstruction of a different sample. The holograms were recorded with the optical tweezer incorporated digital holographic microscope and they are shown in the left column. The first and the second rows show holograms of two yeast samples and their reconstruction at 4cm and 4.5cm respectively. The third row shows the hologram of multiple polystyrene spheres and it's reconstruction at 5cm. The last row show the hologram of the photo-resist structure and it's reconstruction at 3cm.

5.3.2 Trapping and Manipulation of Polystyrene Spheres

The first optical tweezer experiments were conducted without holographic imaging. In order to block the reference wave, a shutter was placed on the reference path and only the intensity of the focused object wave was imaged.

In optical tweezer experiments, $1\mu m$ diameter polystyrene spheres were used as the sample particles as they proved to be excellent testing candidates for the initial

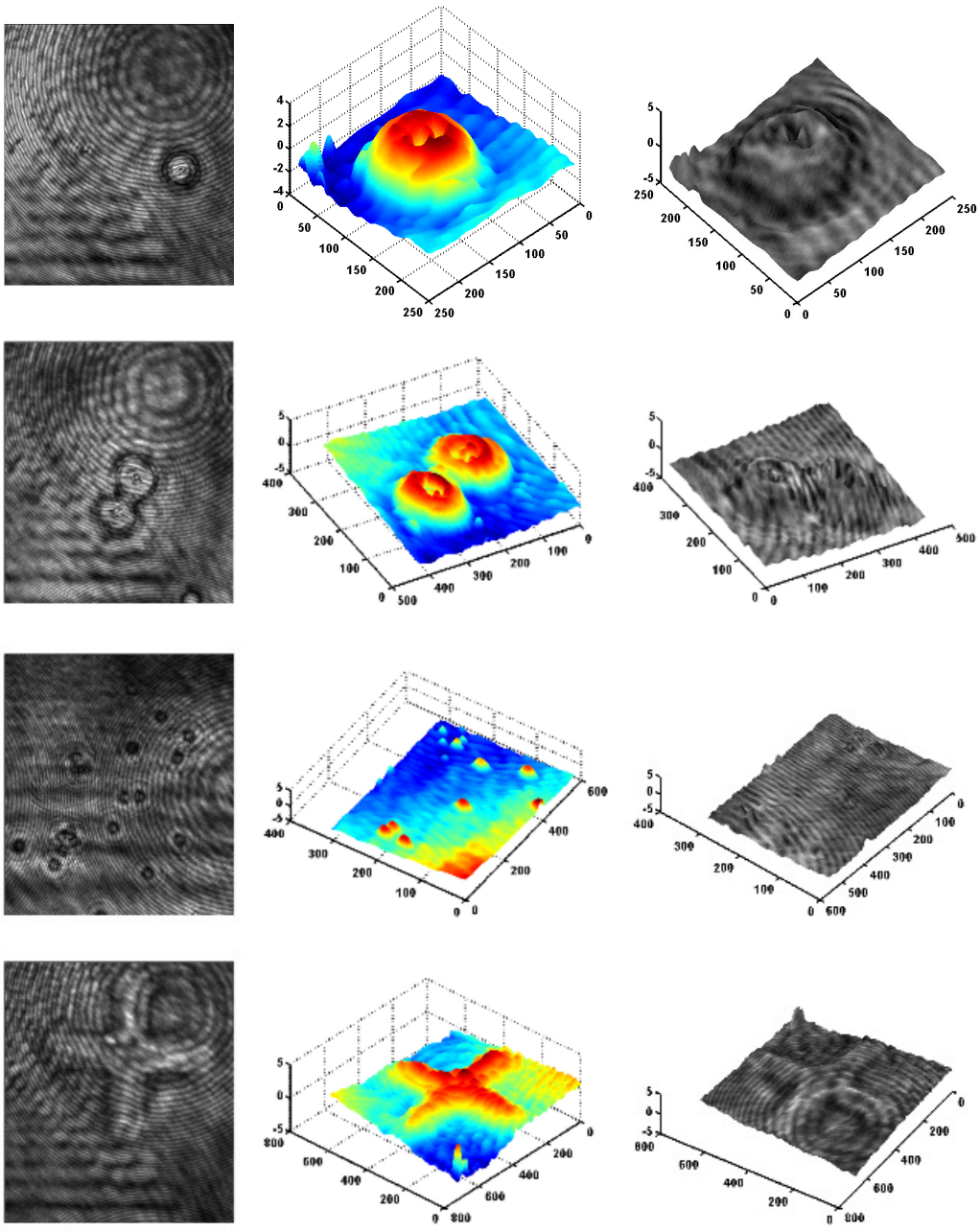

Figure 5.11: The figure shows various holograms and their reconstructions. The images at the left column are the holograms and the remaining images are the focused reconstructions respectively.

tweezers experiments. The spheres were suspended in an aqueous solution which delayed their sticking against the microscope slide and it was possible to use the samples for about a day before the sample dried. After this period most of the spheres became stuck to the microscope slide and it became impossible to manipulate.

Figure 5.12 shows the result of the time-shared trapping experiment where the trap is moved along a pre-defined path to manipulate multiple particles. In this specific experiment, the tweezer coils were driven with sinusoidal signals to move the tweezer trap along an elliptic path. At sufficiently high frequencies (up to 10Hz) the coils spanned the elliptic path fast enough and created a time-shared trap for the free-floating spheres. Initially, the particles were floating freely inside the fluid. After the tweezer trap started moving periodically, the particles started to line up with the defined path of the tweezer trap in seconds.

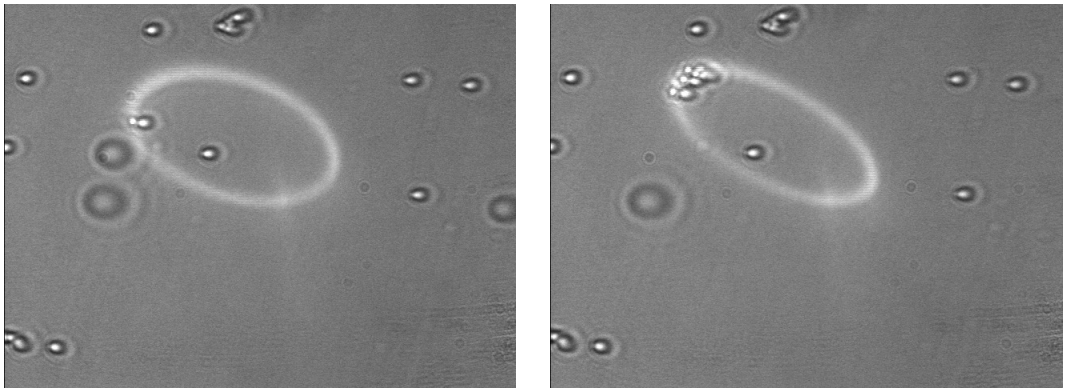

Figure 5.12: The figure shows the result of the time-shared trapping experiment. (a) is the initial image of the sample and (b) is the image after a short period of time. It is clearly seen in (b) that the polystyrene spheres are trapped by the optical tweezer.

In an other experiment, the polystyrene spheres were trapped and dragged along a path defined by a couple of mouse clicks on the screen. The figure 5.13 shows four images of the scene where the dashed lines represents the path of the optical trap. Initially, there were no spheres inside the optical trap; and when the trap moved

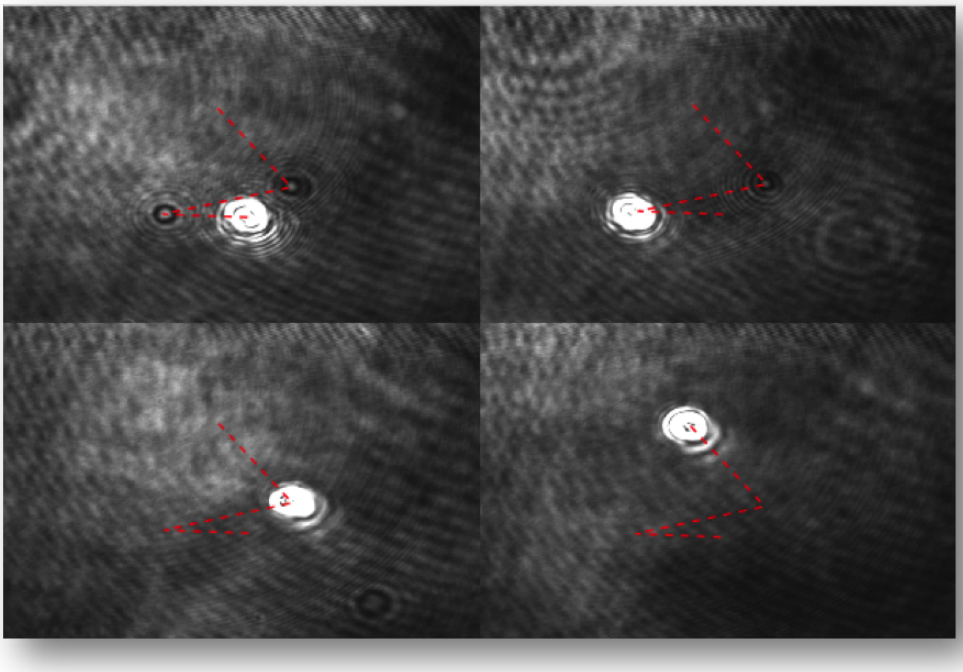

Figure 5.13: The figure shows experiment where the polystyrene spheres are moved along a specific path defined by three mouse clicks.

along the path, the particles were trapped and dragged by the tweezer beam.

Finally, the shutter on the reference arm was opened to enable holographic imaging. The figure 5.14 show a single hologram (left) and a phase-shifted hologram (right) of an empty microscope slide. The bright spot on the left image is caused by tweezer beam. The tweezer trap saturates the pixels of the CCD and distorts the hologram. Due to phase-shifting, the trap becomes black in the phase-shifted hologram.

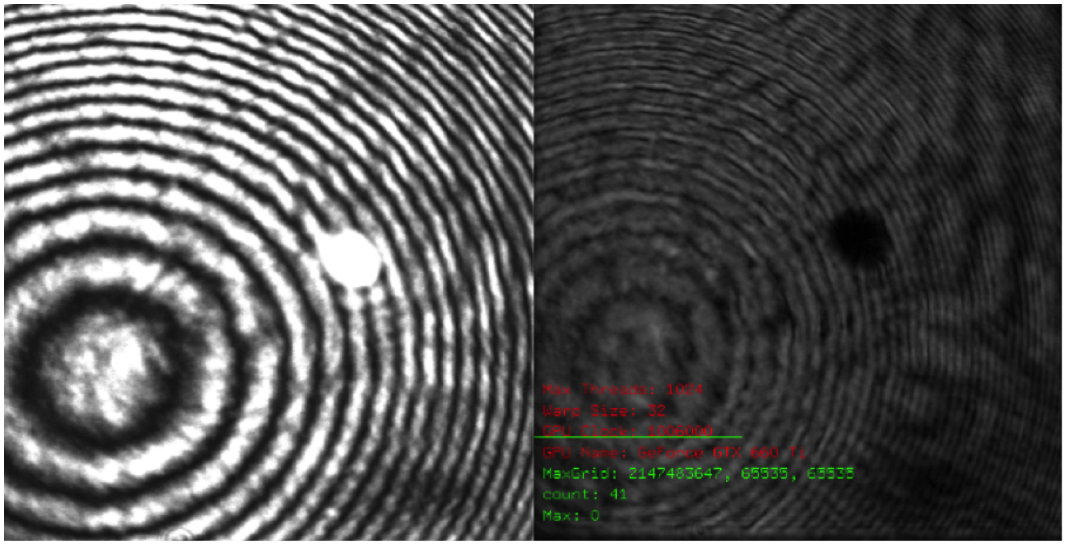

Figure 5.14: The figure shows the interference pattern without a sample and the tweezer beam.

6 CONCLUSION

In this thesis, an auto-focusing megapixels-resolution digital holographic microscope (DHM) that has optical tweezing capability was introduced. First of all, principles of digital holography were covered, and the Fresnel's method, the convolution method and the angular spectrum method were presented. The limitations and the performances of the these three reconstruction methods were compared. Then, an auto-focusing algorithm was presented for estimating the focus distance of the hologram without priori knowledge. In order to operate the microscope in real-time, a graphics processor was incorporated in the microscope to accelerate the calculations. By incorporating a graphics card into the digital holographic microscope, the microscope was able to reconstruct 70 holograms per second with auto-focusing. Also, the comparison of the GPU and the CPU based implementations was presented, and it was shown that with GPUs, the microscope operated approximately 70 times faster. In addition, the holograms of various samples such as the biological cells, the photo-resist structures and the USAF resolution chart were recorded and the reconstructions were presented. It was shows also that, the surface roughness of the photo-resist coating can be measured using a single phase-sifted hologram.

Finally, a setup for incorporating an optical tweezer to the holographic microscope was provided. It was shown that, manipulating a living cell without destructing it's structure was achieved by the use of an optical tweezer. Also with this setup, it was possible to move and trap small particles while performing holographic imaging.

Bibliography

[1] D. Gabor, "A new microscopic principle," *Nature*, vol. 161, pp. 777–778, 1948.

[2] R. G. Gould, "The laser, light amplification by stimulated emission of radiation," in *The Ann Arbor Conference on Optical Pumping*, 1959, p. 128.

[3] E. N. Leith and J. Upatnieks, "Reconstructed wavefronts and communication theory," *J. Opt. Soc. Am.*, vol. 52, no. 10, pp. 1123–1128, October 1962.

[4] Y. N. Denisyuk, "Photographic reconstruction of the optical properties of an object in its own scattered radiation field," *Soviet Physics Doklady*, vol. 7, p. 543, December 1962.

[5] R. L. Powell and K. A. Stetson, "Interferometric vibration analysis by wavefront reconstruction," *J. Opt. Soc. Am.*, vol. 55, no. 12, pp. 1593–1597, December 1965.

[6] A. Macovski, S. D. Ramsey, and L. F. Schaefer, "Time-lapse interferometry and contouring using television systems," *Appl. Opt.*, vol. 10, no. 12, pp. 2722–2727, December 1971.

[7] J. Butters and J. Leendertz, "Speckle pattern and holographic techniques in engineering," *Optics and Laser Technology*, vol. 3, no. 1, pp. 26 – 30, 1971.

[8] B. R. Brown and A. W. Lohmann, "Computer-generated binary holograms," *IBM J. Res. Dev.*, vol. 13, no. 2, pp. 160–168, March 1969.

[9] T. Huang, "Digital holography," *Proceedings of the IEEE*, vol. 59, no. 9, pp. 1335–1346, September 1971.

[10] M. A. Kronrod, N. S. Merzlyakov, and L. P. Yaroslavsky, "Reconstruction of a hologram with a computer," *Soviet Physics-Technical Physics*, vol. 17, no. 2, pp. 419–420, 1972.

[11] U. Schnars and W. P. O. Jüptner, "Digital recording of holograms by a cd target and numerical reconstruction," *App. Opt.*, vol. 33, no. 2, pp. 179–181, 1994.

[12] T. Lenart and V. Owall, "Xstream - a hardware accelerator for digital holographic imaging," in *Electronics, Circuits and Systems, 2005. ICECS 2005. 12th IEEE International Conference on*, December 2005, pp. 1–4.

[13] T. Lenart, V. Öwall, M. Gustafsson, M. Sebesta, and P. Egelberg, "Accelerating signal processing algorithms in digital holography using an fpga platform," in *Field-Programmable Technology (FPT), 2003. Proceedings. 2003 IEEE International Conference on*, December 2003, pp. 387–390.

[14] T. Ito, N. Masuda, K. Yoshimura, A. Shiraki, T. Shimobaba, and T. Sugie, "Special-purpose computer horn-5 for a real-time electroholography," *Opt. Express*, vol. 13, no. 6, pp. 1923–1932, March 2005.

[15] T. Shimobaba, Y. Sato, J. Miura, M. Takenouchi, and T. Ito, "Real-time digital holographic microscopy using the graphic processing unit," *Opt. Express*, vol. 16, no. 16, pp. 11 776–11 781, August 2008.

[16] L. Ahrenberg, A. Page, B. Hennelly, J. McDonald, and T. Naughton, "Using commodity graphics hardware for real-time digital hologram view-reconstruction," *Journal of Display Technology*, vol. 5, no. 4, pp. 111 –119, April 2009.

[17] M. Doğar, H. A. İlhan, and M. Özcan, "Real-time, auto-focusing digital holographic microscope using graphics processors," *Review of Scientific Instruments*, vol. 84, no. 8, 2013.

[18] Y. Frauel, T. Naughton, O. Matoba, E. Tajahuerce, and B. Javidi, "Three-dimensional imaging and processing using computational holographic imaging," *Proceedings of the IEEE*, vol. 94, no. 3, pp. 636–653, March 2006.

[19] J. W. Goodman, *Introduction to Fourier Optics*, 2nd ed. New York: McGraw–Hill Companies, Inc., 1996.

[20] R. Dndliker and K. Weiss, "Reconstruction of the three-dimensional refractive index from scattered waves," *Optics Communications*, vol. 1, no. 7, pp. 323 – 328, 1970.

[21] E. N. Leith and J. Upatnieks, "Holographic imagery through diffusing media," *J. Opt. Soc. Am.*, vol. 56, no. 4, pp. 523–523, April 1966.

[22] A. Yariv, "Phase conjugate optics and real-time holography," *Quantum Electronics, IEEE Journal of*, vol. 14, no. 9, pp. 650–660, September 1978.

[23] Z. Yaqoob, D. Psaltis, M. S. Feld, and C. Yang, *Nat Photon*.

[24] H. Coufal, G. Sincerbox, and D. Psaltis, *Holographic data storage*. Springer Verlag New York, Inc., 2000.

[25] L. Hesselink, S. S. Orlov, and M. Bashaw, "Holographic data storage systems," *Proceedings of the IEEE*, vol. 92, no. 8, pp. 1231–1280, August 2004.

[26] L. Onural, A. Gotchev, H. Özaktas, and E. Stoykova, "A survey of signal processing problems and tools in holographic three-dimensional television," *Circuits*

and Systems for Video Technology, IEEE Transactions on, vol. 17, no. 11, pp. 1631–1646, November 2007.

[27] Y. Takaki, H. Kawai, and H. Ohzu, "Hybrid holographic microscopy free of conjugate and zero-order images," *App. Opt.*, vol. 38, pp. 4990–4996, August 1999.

[28] P. Langehanenberg, B. Kemper, D. Dirksen, and G. von Bally, "Autofocusing in digital holographic phase contrast microscopy on pure phase objects for live cell imaging," *Applied Optics*, vol. 47, no. 19, pp. 176–182, 2008.

[29] Y. Sun, S. Duthaler, and B. J. Nelson, "Autofocusing in computer microscopy: selecting the optimal focus algorithm," *Microscopy Research and Technique*, vol. 65, pp. 139–149, October 2004.

[30] I. Yamaguchi, J. ichi Kato, S. Ohta, and J. Mizuno, "Image formation in phase-shifting digital holography and applications to microscopy," *Appl. Opt.*, vol. 40, no. 34, pp. 6177–6186, December 2001.

[31] A. Ashkin, "Acceleration and trapping of particles by radiation pressure," *Phys. Rev. Lett.*, vol. 24, pp. 156–159, January 1970.

[32] E. Cuche, P. Marquet, and C. Depeursinge, "Spatial filtering for zero-order and twin-image elimination in digital off-axis holography," *Appl. Opt.*, vol. 39, no. 23, pp. 4070–4075, August 2000.

[33] M. Özcan and M. Bayraktar, "Digital holography image reconstruction methods," in *Proc. of SPIE*, vol. 72330B-1, 2009.

[34] T. Tahara, K. Ito, T. Kakue, M. Fujii, Y. Shimozato, Y. Awatsuji, K. Nishio, S. Ura, T. Kubota, and O. Matoba, "Parallel phase-shifting digital holographic microscopy," *Biomed. Opt. Express*, vol. 1, no. 2, pp. 610–616, September 2010.

[35] Y. Awatsuji, M. Sasada, A. Fujii, and T. Kubota, "Scheme to improve the reconstructed image in parallel quasi-phase-shifting digital holography," *Appl. Opt.*, vol. 45, no. 5, pp. 968–974, February 2006.

[36] Y. Awatsuji, A. Fujii, T. Onchi, T. Kubota, and O. Matoba, "Parallel three-step-phase-shifting digital holography," in *Adaptive Optics: Analysis and Methods/Computational Optical Sensing and Imaging/Information Photonics/Signal Recovery and Synthesis Topical Meetings on CD-ROM*. Optical Society of America, 2005, p. JWB4.

[37] U. Schnars and W. P. O. Jüptner, "Digital recording and numerical reconstruction of holograms," *App. Opt.*, vol. 41, no. 5, pp. 853–864, 2002.

[38] T. M. Kreis, M. Adams, and W. P. O. Jüptner, "Methods of digital holography: a comparison," in *Proc. SPIE*, vol. 3098, 1997, pp. 224–233.

[39] M. Doğar, H. A. İlhan, and M. Özcan, "Real-time reconstruction of digital holograms with gpu," in *Proc. SPIE*, vol. 8644, 2013, pp. 86 440B–86 440B–8.

[40] H. A. İlhan, M. Doğar, and M. Özcan, "Fast autofocusing in digital holography using scaled holograms," *Optics Communications*, vol. 287, pp. 81–84, 2013.

[41] F. Dubois, C. Schockaert, N. Callens, and C. Yourassowsky, "Focus plane detection criteria in digital holography microscopy by amplitude analysis," *Opt. Express*, vol. 14, pp. 5895–5908, June 2006.

[42] F. C. Groen, I. T. Young, and G. Ligthart, "A comparison of different focus functions for use in autofocus algorithms," *Cytometry*, vol. 6, pp. 81–91, 1985.

[43] R. A. Muller and A. Buffington, "Real-time correction of atmospherically degraded telescope images through image sharpening," *Opt. Soc. Am.*, vol. 64, pp. 1200–1210, 1974.

[44] S. Yazdanfar, K. B. Kenny, K. Tasimi, A. D. Corwin, E. L. Dixon, and R. J. Filkins, "Simple and robust image-based autofocusing for digital microscopy," *Optics Express*, vol. 16, no. 12, pp. 8670–8677, June 2008.

[45] L. Orzo, Z. Gorocs, I. Szatmari, and S. Tokes, "Gpu implementation of volume reconstruction and object detection in digital holographic microscopy," in *Cellular Nanoscale Networks and Their Applications (CNNA), 2010 12th International Workshop on*, February 2010, pp. 1 –4.

[46] D. Kirk and W. Hwu, *Programming Massively Parallel Processors: A Hands-on Approach*, ser. Applications of GPU Computing Series. Elsevier Science, 2010.

[47] A. Krejcir, "Image reconstruction in digital holographic microscopy on GPU," Master's thesis, Masarykova Univerzita Fakulta Informatiky, Brno, 2013.

[48] V. Demir and A. Elsherbeni, "Utilization of cuda-opengl interoperability to display electromagnetic fields calculated by FDTD," in *Computational Electromagnetics International Workshop (CEM), 2011*, aug. 2011, pp. 95 –98.

[49] K. Nanda, S. Sarangi, and S. Sahu, "Measurement of surface roughness by atomic force microscopy and rutherford backscattering spectrometry of cds nanocrystalline films," *Applied Surface Science*, vol. 133, no. 4, pp. 293 – 297, 1998.